2007

Late Cretaceous to Paleocene Metamorphism and Magmatism in the Funeral Mountains Metamorphic Core Complex, Death Valley, California

Chris G. Mattinson
Stanford University, mattinson@geology.cwu.edu

Joseph P. Colgan
Stanford University

James R. Metcalf
Stanford University

Elizabeth L. Miller
Stanford University

Joseph L. Wooden
U.S. Geological Survey

Follow this and additional works at: http://digitalcommons.cwu.edu/cotsfac

Part of the Geochemistry Commons, Geomorphology Commons, and the Tectonics and Structure Commons

Recommended Citation

Late Cretaceous to Paleocene metamorphism and magmatism in the Funeral

Mountains metamorphic core complex, Death Valley, California

Christopher G. Mattinson, Joseph P. Colgan, James R. Metcalf, and Elizabeth L. Miller

Department of Geological and Environmental Sciences, Stanford University, Stanford,

California 94305, USA

Joseph L. Wooden

United States Geological Survey, 345 Middlefield Road, Menlo Park, California 94025,

USA

ABSTRACT

Amphibolite facies Proterozoic metasedimentary rocks below the low-angle Cenozoic Boundary Canyon detachment (BCD) record deep crustal processes related to Mesozoic crustal thickening and subsequent extension. A 91.5 ± 1.4 Ma Th/Pb SHRIMP-RG monazite age from garnet-kyanite-staurolite schist constrains the age of prograde metamorphism in the lower plate. Between the BCD and the structurally deeper, subparallel Monarch Spring fault (MSF), prograde metamorphic fabrics are overprinted by a pervasive greenschist-facies retrogression, high strain subhorizontal mylonitic foliation, and a prominent WNW-ESE stretching lineation parallel to corrugations on the BCD. Granitic pegmatite dikes are deformed, rotated into parallelism and boudinaged within the mylonitic foliation. High-U zircons from one muscovite granite dike yield an 85.8 ± 1.4 Ma age. Below the MSF, retrogression is minor, and

amphibolite-facies mineral elongation lineations plunge gently N-NE. Multiple generations of variably deformed dikes, sills, and leucosomal segregations indicate a more complex history of partial melting and intrusion compared to that above the MSF, but thermobarometry on garnet amphibolites above and below the MSF record similar peak conditions of 620 to 680°C, 7 to 9 kbar, indicating minor (<3 to 5 km) structural omission across the MSF. Discordant SHRIMP-RG U/Pb zircon ages and 75 to 88 Ma Th/Pb monazite ages from leucosomal segregations in paragneisses suggest partial melting of Proterozoic sedimentary protoliths was a source for the structurally higher 86 Ma pegmatites. Two weakly deformed two-mica leucogranite dikes that cut the high-grade metamorphic fabrics below the MSF yield 62.3 ± 2.6 and 61.7 ± 4.7 Ma U/Pb zircon ages, and contain 1.5 to 1.7 Ga cores. The similarity of metamorphic, leucosome, and pegmatite ages to the period of Sevier belt thrusting and the period of most voluminous Sierran arc magmatism suggests that both burial by thrusting and regional magmatic heating contributed to metamorphism and subsequent partial melting.

INTRODUCTION

Cenozoic metamorphic core complexes in the western United States (Fig. 1) commonly overprint and obscure older metamorphic fabrics and structures developed during Mesozoic deformation and magmatism (e.g., Miller and Gans, 1989; Wells and Allmendinger, 1990). High-grade metamorphic rocks exposed in core complexes directly record deep-crustal processes operating during Mesozoic crustal thickening, and reveal

the relation between supracrustal thrust faulting in the Sevier fold and thrust belt, and lower crustal metamorphism, magmatism, and deformation. In addition, differentiating between these deformational events is critical for understanding the magnitude and rate of Tertiary Basin and Range extension (e.g., Hodges and Walker, 1992; Miller and Gans, 1989; Miller et al., 1999).

In the northern Funeral Mountains of Death Valley (Figs. 1 and 2), the Boundary Canyon Detachment (BCD) separates low to subgreenschist-facies Proterozoic sedimentary rocks in the upper plate from greenschist- to amphibolite-grade metamorphic rocks in the lower plate of the Funeral Mountains metamorphic core complex (Labotka, 1980; Giaramita, 1984; Hoisch and Simpson, 1993; Wright and Troxel, 1993). Lower-plate metamorphism is poorly constrained as Mesozoic (e.g., DeWitt, 1988; Labotka, 1980), and the BCD was active as recently as the late Miocene (Reynolds et al., 1986; Holm and Dokka, 1991; Wright and Troxel, 1993). Lower-plate minerals, textures, and fabrics formed during Mesozoic metamorphism are overprinted by prominent greenschist-facies extensional fabrics that strongly mylonitized the quartzites and marbles in the lower plate of the BCD near Monarch Canyon (Giaramita, 1984; Hoisch and Simpson, 1993). In Monarch Canyon (Figs. 1 and 2), amphibolite-facies lower plate rocks are intruded by at least two generations of variably deformed granitic and pegmatite dikes. Based on U-Pb ages and cross-cutting relationships, Applegate et al. (1992) and Applegate and Hodges (1995) suggested that the prominent ductile extensional fabrics in the footwall of the BCD record a major episode of Cretaceous (70 to 72 Ma) extension across the Cordilleran orogen (e.g., Hodges and Walker, 1992) unrelated to later development of the low angle, metamorphic core complex detachment

fault(s). In contrast, Hoisch and Simpson (1993) suggested that the ductile fabrics related to vertical thinning developed concurrently with slip on the BCD as lower plate rocks rose and cooled during the late Tertiary (21 to 6 Ma).

This study applies field and thin-section observations, thermobarometry, and SHRIMP U-Th-Pb monazite and zircon geochronology on a suite of representative, well-preserved samples to constrain the timing and conditions of peak metamorphism and magmatism in the lower plate of the Funeral Mountains metamorphic core complex. We use these data to reexamine the temporal relationship between Mesozoic metamorphic fabrics and superimposed, younger extension-related fabrics in the Monarch Canyon area.

GEOLOGIC SETTING

In the northern Funeral Mountains, amphibolite-grade metamorphic rocks are exposed in a doubly plunging anticline with structurally deepest levels exposed in Monarch Canyon (Figs. 1 and 2; Giaramita, 1984; Wright and Troxel, 1993; Applegate, 1994); metamorphic grade decreases to the southeast (Labotka, 1980). The peak metamorphic assemblage of lower-plate units is kyanite + staurolite + biotite + garnet in pelitic schists, and hornblende + plagioclase + garnet in mafic rocks. Pelites locally contain sillimanite in the core of Monarch Canyon (Figs. 1 and 2). Lower plate metamorphic rocks are separated from low to subgreenschist-facies Proterozoic strata and unmetamorphosed Tertiary sedimentary and volcanic rocks to the northeast by the gently northeast-dipping Boundary Canyon Detachment (BCD), and to the southwest by the moderately southwest-dipping Keane Wonder fault zone (Wright and Troxel, 1993; Fig.

1). Hamilton (1988) and Hoisch and Simpson (1993) regard these two faults as traces of a single, domiform detachment fault, but Wright and Troxel (1993) and Applegate and Hodges (1995) consider these structures to have evolved separately. In outcrop, there is a strong contrast between the nature of the BCD (sharp contact, chlorite microbreccia, but no widespread breccia or gouge) and the broad zone of fault breccia and gouge characteristic of the Keane Wonder fault zone. Based on these observations, we infer that the BCD is an older structure truncated by more recent slip on the Keane Wonder fault (e.g., Applegate and Hodges, 1995).

Similarities in the timing of events, the structures developed, and metamorphic grade of exposed rocks led Hamilton (1988), Hoisch et al. (1997), and Hoisch (2000) to link the BCD with similar low angle detachment faults north and northeast of the Funeral Mountains in the Bullfrog Hills and Bare Mountain. As in the Funeral Mountains, metamorphic grade increases to the northwest from lower greenschist (slaty pelites to non-marbleized carbonates) in the south of Bare Mountain to lower amphibolite (staurolite + garnet) in the northwest, and finally amphibolite (staurolite + kyanite) in the Bullfrog Hills (Hamilton, 1988). A geothermal gradient of 27°C/km for peak conditions in the lower plate rocks of Bare Mountain is consistent with our estimates in Monarch Canyon (see below; Hoisch, 2000).

Description of Lower Plate units

The lower plate consists of marbles, quartzites, and schists correlated with the

Johnnie Formation and the underlying 1.1 Ga Pahrump Group (Wright and Troxel, 1993), which we have divided into four tectonostratigraphic units (Fig. 2).

Pelitic schist (Zjl)   The uppermost unit (Zjl), bounded above by the BCD and below by the Chloride Cliff fault (Fig. 2), consists of pelitic schist with layers of amphibolite and pebbly quartzite that Wright and Troxel (1993) correlate with the lower member of the Late Proterozoic Johnnie Formation. Near its base above the Chloride Cliff fault we include a variety of grey calcite marbles, orange-weathering impure silty marbles, calc-schists, and calcareous conglomerates. These probably correlate with the Late Proterozoic Noonday Dolomite and Kingston Peak Formation (Applegate, 1994; Applegate and Hodges, 1995).

Beneath the BCD, this unit contains a thick section of chloritized pelitic schist with a prominent extensional crenulation cleavage that overprints an older schistose fabric. Metamorphic porphyroblasts are mostly replaced by clots of chlorite and sericite, but sparse garnet + staurolite + kyanite porphyroblasts are preserved at even the highest structural levels beneath the BCD, and amphibolites are garnet-bearing.

Calcite marbles (Ycl) Below the Chloride Cliff fault is a cliff-forming grey to buff calcite marble (Ycl) that forms a prominent marker horizon (Fig. 2). This highly-deformed unit crops out as calc-mylonite with a conspicuous stretching lineation (oriented ~N60º W; Fig. 3), that is defined by light and dark streaks on foliation surfaces. Applegate (1994) and Applegate and Hodges (1995) correlate this unit with the Middle Proterozoic Beck Spring Dolomite.

Silty marble (Ycm) and Pelitic Schists (Ycs) A heterogeneous unit (Ycm) comprising a thick succession of dark-weathering ledge- and cliff-forming calcareous schists with thin, impure orange-weathering marble layers underlies the calcite marble (Ycl). Underlying the Ycm unit are pelitic schists (Ycs) with thin amphibolites and minor marble and quartzite. The base of the Ycs unit contains dark-weathering calc-schists, amphibolites, marbles, and quartzites. Quartzites at the base of this section are well-developed mylonites with conspicuous S-C fabrics, grain-shape foliations, and lattice preferred orientations in thin section. Fabrics and their orientations (Fig. 3) indicate extreme thinning and NW-SE extension with a top-to-the-NW sense of shear, which is parallel to shear sense indicators in quartz and marble mylonite as much as 300 m structurally beneath the BCD (Hoisch and Simpson, 1993). Applegate (1994) and Applegate and Hodges (1995) correlate the Ycm and Ycs units with the Middle Proterozoic Crystal Spring Formation.

The base of the Ycm-Ycs unit is defined by a previously unmapped ductile to brittle fault, which we informally call the Monarch Spring fault (MSF; Fig. 2). The MSF truncates more steeply dipping compositional layering beneath it (Fig. 4A), and rocks immediately above and along this contact record high strains (quartz mylonites and cataclastic deformation; Fig. 4B). Sense of shear fabrics along the contact and bending of underlying layers into the contact indicate top-to-the-NW motion. The MSF cuts down structural section in its direction of motion, and truncates and bends layers beneath it.

High-grade gneisses and migmatites (Xmi) Below the MSF, the deepest exposed

unit (Xmi) consists of thinly banded (<10 cm), strongly compositionally layered gneisses composed of hornblende- and biotite-rich gneiss, pelitic gneiss and migmatite (locally sillimanite-bearing), amphibolite, and small leucogranitic bodies. Wright and Troxel (1993) interpreted these rocks to be Precambrian crystalline basement based on a 1.7 Ga zircon U-Pb age from a granitic dike (R.E. Zartman [1985], cited in Wright and Troxel, 1993). In contrast, Giaramita (1984), Applegate (1994), and Applegate and Hodges (1995) interpreted these rocks as metamorphosed equivalents of the lower Crystal Spring Formation. The gneisses contain thin calc-silicate and sparse marble layers, leading us to follow Giaramita (1984) and Applegate (1994) in assigning this unit (Xmi; Fig. 2) to the lower Crystal Spring Formation (Middle Proterozoic) rather than to Precambrian crystalline basement (e.g. Wright and Troxel, 1993).

Gneissic fabrics in this unit are truncated by the MSF at a high angle (Fig. 4A), and (with the exception of some quartz-rich layers) these rocks conspicuously lack the prominent mylonitic fabric developed in rocks above the MSF (Fig. 3). This unit is more mafic and contains significantly more intrusive rocks than units above the MSF. The abundance of cross-cutting granitic dikes, migmatites, biotite and hornblende, the presence of sillimanite, and the discordant structural fabrics all suggest that these rocks record a somewhat different metamorphic and deformational history from those above the MSF. Lineations below the MSF are defined by the peak metamorphic assemblage (measured mostly on aligned hornblende in amphibolite layers), and trend NE (Fig. 3). In contrast, lineations of the mylonitic fabric above the MSF trend WNW-ESE (Fig. 3) and developed at greenschist-facies parallel to other extensional structures, including low-temperature ductile microfabrics and asymmetric folds (Hoisch and Simpson, 1993)

and large-scale corrugations on the BCF (Fig. 3).

Lower Plate Metamorphism

Variable, but widespread greenschist-facies retrogression and hydrothermal alteration (mapped by Labotka, 1980) is most strongly developed at high structural levels near the BCD, but is also evident in pelitic schist between the BCD and MSF. Pelitic schist of the Johnnie Formation is deformed by an extensional crenulation cleavage below the BCD. Above the MSF, garnet porphyroblasts preserve rotated inclusion trails (Fig. 5B, D), indicative of late syntectonic growth. Below the MSF, garnet porphyroblasts contain few inclusions, which do not define an internal foliation (Fig. 5C, E), and the rocks are dominated by annealed or static recrystallization textures consistent with their structurally lower position. Rocks below the MSF show little evidence for the pervasive retrogression and associated strain exhibited by the overlying units.

Metamorphic rocks in the northern Funeral Mountains are intruded by several generations of granitic dikes, most abundant near Monarch Canyon, decreasing in abundance to the southeast, and nearly absent beyond Chloride Cliff (Hoisch and Simpson, 1993). Above the MSF, these dikes were deformed under greenschist-facies conditions, boudinaged, and rotated into parallelism with the mylonitic foliation (Figs. 3 and 4D). Below the MSF, the metamorphic rocks preserve an older fabric (Fig. 3), and the greenschist-facies retrogression and strong mylonitic foliation are largely absent. Here, strongly deformed dikes and sills approximately parallel to foliation and involved in folding are cut by younger, less deformed dikes (Fig. 4C). The older dikes are

typically pegmatitic, with coarse-grained (>2 cm) books of muscovite, whereas the younger dikes are typically finer-grained (<2 mm) two-mica granites. The difference in grain size, mineral assemblage, and relation to foliation and folds suggests that the dikes represent (at least) two distinct episodes of melt generation. Both sets of dikes appear to post-date leucosomal segregations in migmatitic rocks, but the absence of chilled margins and some "mingling" of dikes with leucosomes suggests intrusion while the host rocks were still very hot, and possibly partially molten. All fabrics are prominently cut by sparse mafic dikes (Fig. 4B) which postdate all ductile deformation.

Metamorphic petrology and isograd mapping (Labotka, 1980; Giaramita, 1984; Labotka and Albee, 1988; Hoisch and Simpson, 1993) indicate that kyanite zone pelitic schists in Monarch Canyon record peak conditions of 7.2 to 9.6 kbar, and 600 to 700°C (Labotka, 1980), similar to estimates of 7.6 to 9.1 kbar, and 670 to 700°C reported by Hoisch (1991). Hodges and Walker (1990) reported similar peak pressures of 8 to 10 kbar, but considerably lower temperatures (525 to 575°C). The presence of sillimanite in pelitic gneisses at the deepest exposed levels support the higher temperature estimates. The common occurrence of kyanite is consistent with the thermobarometric determinations, which indicate peak conditions in the kyanite field; Hoisch and Simpson (1993) suggest that sillimanite may have formed during decompression.

TIMING OF DEFORMATION AND METAMORPHISM

The timing of peak metamorphism is not well known. Labotka (1980) suggested that metamorphism was contemporaneous with late Mesozoic metamorphism in the

Panamint Mountains. DeWitt et al. (1988) suggested an Early Cretaceous age (>115 to 130 Ma) for metamorphism based on disturbed hornblende $^{40}Ar/^{39}Ar$ spectra. Applegate (1994) reported a poorly constrained 127 ± 9 Ma lower intercept for strongly discordant zircon U-Pb analyses from a kyanite-garnet mica schist in the lower Crystal Spring Formation in Monarch Canyon, which was interpreted to record Early Cretaceous metamorphism.

Granitic dikes, initially regarded as either Precambrian (1.7 Ga zircon U-Pb, R.E. Zartman [1985], cited in Wright and Troxel, 1993), or possibly Tertiary (30 Ma muscovite K-Ar, Wasserburg et al., 1959), are considered to constrain the minimum age of metamorphism (Labotka and Albee, 1988). Applegate et al. (1992) reported zircon and monazite U-Pb ages for two generations of pegmatite dikes, 70 and 72 Ma, respectively. Subsequently, Applegate (1994) determined younger ages from the deformed dikes of 66 to 64 Ma. As noted by Applegate et al. (1992) and Applegate (1994), post-crystallization Pb-loss is likely for these samples due to extensive radiation damage from the high (>2000 ppm) U concentrations in the zircons. Therefore, these ages are probably minimum constraints on pegmatite crystallization ages. Two additional samples of undeformed dikes analyzed by Applegate (1994) did not yield concordant analyses; regression indicates ca. 1.7 Ga inheritance and a poorly constrained 80 ± 70 Ma lower intercept. A third sample of an undeformed dike yielded a reversely discordant 54 Ma age; high (>4000 ppm) U in this fraction suggests radiation-damage-related Pb-loss, and this age probably also represents a minimum constraint on the crystallization age (Applegate, 1994).

Titanite, zircon, and apatite fission track thermochronology suggest rapid cooling

from T>285°C at 9 to 10 Ma (Holm and Dokka, 1991). $^{40}Ar/^{39}Ar$ and conventional K-Ar thermochronology on amphibole, muscovite, biotite, and K-feldspar (DeWitt et al., 1988; Hoisch and Simpson, 1993; Applegate, 1994) reveal complicated spectra indicative of excess argon. Applegate (1994) interpreted scattered Late Cretaceous to Miocene muscovite and biotite $^{40}Ar/^{39}Ar$ ages to reflect extended residence near the closure temperature and slow cooling prior to the rapid mid- to late Miocene cooling documented by fission track (Holm and Dokka, 1991) and K-feldspar $^{40}Ar/^{39}Ar$ (Applegate, 1994) thermochronology. Hoisch and Simpson (1993) interpreted the variability in $^{40}Ar/^{39}Ar$ and K-Ar age for a specific mineral to reflect excess Ar, and therefore used the minimum measured age as a maximum age constraint (21 Ma for muscovite) on cooling.

MINERAL CHEMISTRY

Garnet in most amphibolites is $Alm_{45-65}Sps_{1-10}Prp_{5-13}Grs_{20-41}$, although biotite-rich sample MCGM-1B is richer in Prp (11 to 21 mol%) and lower in Grs (12 to 15 mol%). Samples MC-A and MCGM-8B, below the MSF, contain garnet with the highest Grs content (32 to 41 mol%; Tables 1, 2; Appendix A; Fig. 6B), contain epidote, and occur as thin bands within pelitic gneiss. Samples MC-B and MC-E, above the MSF, contain garnet lower in Grs (22 to 28 mol%; Table 2; Fig. 6A), and occur as m-scale boudins within pelitic schist, which suggests a different protolith, such as a basaltic dike or flow (e.g., Giaramita, 1984). Garnet in pelitic gneiss MCGM-9 is $Alm_{71-80}Sps_{5-10}Prp_{9-17}Grs_{3-4}$. Compositional zoning profiles are shown in Fig. 6. Sample MC-E, above the MSF, has a bell-shaped Mn profile (Fig. 6A), which probably reflects growth zonation (Spear, 1995),

partially modified by diffusion. Below the MSF, sample MCGM-8B preserves zoning (Fig. 6B), but profiles of the smaller garnets in samples MCGM-1B (Fig. 6C) and MCGM-5 (Fig. 6D), are flat in the interior, which suggests that these small grains were homogenized by equilibration at high temperatures, and the increase in Mn and Fe/Mg near the rim indicates retrograde diffusion and minor garnet resorption.

Hornblende is unzoned in most samples; some grains show a very slight Fe/Mg increase next to garnet. Compositions lie in the ferropargasite, ferrotschermakite, tschermakite, and magnesiohornblende fields (site assignments, Fe^{3+} estimation, and classification follow Leake et al. 1997). The $Mg/(Mg + Fe^{2+}) = 0.34$ to 0.56, and $Fe^{3+}/(Al + Fe^{3+})$ is <0.1 in most samples, but is up to 0.23 in MCGM-5, consistent with the relatively oxidized conditions suggested by the presence of epidote and magnetite (Table 1).

Plagioclase compositions vary within and among grains, but lack systematic zoning. The plagioclase in garnet-sillimanite gneiss MCGM-9 shows little compositional variation. The most extreme plagioclase compositional variation is in garnet amphibolite MC-A, which contains homogeneous An_{82} plagioclase cross-cut and partially rimmed by zoned An_{37-41} plagioclase.

THERMOBAROMETRY

Mineral thermobarometry of garnet amphibolites above and below the MSF was performed to constrain the P-T conditions of metamorphism recorded by samples above and below the MSF. Pressure and temperature during metamorphism were estimated using (1) the THERMOCALC 3.1 program of Holland and Powell (1998), with activities

calculated by the AX program of Holland and Powell (1998), and (2) temperature estimates using the garnet-hornblende Fe-Mg exchange thermometer of Graham and Powell (1984) combined with the garnet-hornblende-plagioclase-quartz barometers of Kohn and Spear (1990), with additional temperature estimates using the hornblende-plagioclase thermometers of Holland and Blundy (1994). In one sample (MCGM-5), the garnet-ilmenite Fe-Mn exchange thermometer of Pownceby et al. (1987) was applied to an ilmenite inclusion within garnet. Mineral compositions (Table 2) lie within the calibration range of the thermobarometers, except for the An_{82} plagioclase in sample MC-A, which lies above the An_{15-70} range for the Kohn and Spear (1990) barometers, and the amphibole in sample MCGM-5, which lies above the Fe/(Fe + Mg) = 0.4 to 0.6 range of the Kohn and Spear (1990) barometers.

Garnet and hornblende analyses selected for thermobarometry are near the grain rims, but outside steep near-rim zoning (where present). Calculated pressures are sensitive to the Ca partitioning between garnet and plagioclase, and plagioclase compositions include maximum and minimum anorthite contents to assess the uncertainty in the pressure estimate due to plagioclase compositional variability.

Pressure-temperature estimates are listed in Table 3, and plotted in Fig. 7. Estimates based on the intersection of the Graham and Powell (1984) garnet-hornblende thermometer with the Kohn and Spear (1990) barometers generally agree within uncertainty with values derived from THERMOCALC (Holland and Powell 1998). Kohn and Spear (1990) estimate a 0.5 to 1.0 kbar uncertainty for their barometers. Graham and Powell (1984) do not provide an uncertainty estimate for their thermometer, but the ±5% uncertainty of the Ellis and Green (1979) garnet-clinopyroxene thermometry used for its

calibration provides a minimum uncertainty estimate. Holland and Blundy (1994) estimate 35 to 40°C uncertainty associated with their hornblende-plagioclase thermometers. Within uncertainties, the two formulations of the hornblende-plagioclase thermometer (Holland and Blundy, 1994) agree with each other as well as with the Graham and Powell (1984) thermometer and temperature estimates from THERMOCALC (Holland and Powell 1998).

In sample MCGM-5, the Graham and Powell (1984) and Pownceby et al. (1987) temperature estimates are significantly higher than the THERMOCALC temperature estimate, and are also higher than temperature estimates for the other samples. This disagreement may be related to the Fe-rich amphibole composition, which introduces a significant uncertainty in the Fe^{3+} estimate of the amphibole, and Fe^{3+} in ilmenite, which is not accounted for in the Pownceby et al. (1987) thermometer. The Holland and Blundy (1994) thermometers could not be applied to this sample due to its inappropriate composition. Uncertainties associated with P-T estimates for sample MCGM-9 are considerably larger than those for the other samples, and may reflect disequilibrium. This sample contains fibrous sillimanite, but no kyanite, and appears to have undergone partial melting. We therefore regard these P-T estimates as potentially unreliable.

The pressure temperature estimates for all of the samples are consistent with peak conditions of ca. 620 to 680°C and 7 to 9 kbar. These estimates imply a depth of equilibration of 25 to 33 km, assuming an average crustal density of 2.8 g/cc, and correspond to average geothermal gradients of 19 to 27 °C/km, which is normal to slightly elevated relative to a "normal" 20°C/km geotherm (Spear, 1995).

U-Th-Pb GEOCHRONOLOGY

Five samples were analyzed at the Stanford-USGS SHRIMP-RG laboratory; sample preparation and instrument conditions were similar to those described by Williams (1998) and are summarized in Appendix B. Zircon U/Pb ages presented here are ^{207}Pb-corrected ^{206}Pb*/^{238}U ages and uncertainties are 2-sigma unless otherwise noted. Monazites can incorporate significant ^{230}Th (a member of the ^{238}U to ^{206}Pb decay chain) at the time of crystallization, which yields excess ^{206}Pb, resulting in ^{206}Pb*/^{238}U ages that are too old (e.g., Parrish, 1990). The ^{207}Pb*/^{235}U system is free of this effect, but in young samples, low count rates on ^{207}Pb preclude precise age determination. Ages cited below use the ^{204}Pb-corrected ^{208}Pb/^{232}Th system, which gives high count rates in parent and daughter isotopes, yielding precise ratio measurements. Ireland et al. (1999) identified an isobaric interference at m/e = 204 (ThNdO$_2$$^{++}$), which may introduce inaccuracies in ^{204}Pb-corrected isotopic ratios. We did not apply a correction for this interference, but ages derived from corrected and uncorrected ^{208}Pb/^{232}Th ratios are similar, indicating that this effect is smaller than the measurement uncertainty.

Garnet-staurolite-kyanite schist

Sample MCGM-12, from a garnet-staurolite-kyanite schist above the MSF, contains zircon, monazite, and xenotime, both as inclusions in kyanite and in the groundmass. Monazite grains are featureless in BSE (Fig. 8C) and yield a tight grouping of analyses reflecting mixing with common Pb (Table 4; Fig. 10A). We interpret the

weighted mean $^{208}Pb*/^{232}Th$ age of 91.5 ± 1.4 Ma to reflect prograde monazite growth during development of the peak metamorphic assemblage.

Garnet-sillimanite gneiss

Sample JM-DV-3, a strongly-deformed leucosomal segregation within a migmatitic garnet-sillimanite gneiss below the MSF, yields monazite with patchy brightness zones in BSE (Fig. 8D). The $^{208}Pb*/^{232}Th$ ages range from 88 to 75 Ma with one analysis as young as 71 Ma (Table 4; Fig. 10B), and probably reflect mixing of more than one generation of monazite and/or a protracted period of monazite growth, including metamorphism and partial melting event(s). Zircon separated from this sample yields strongly discordant ages (Table 4), consistent with partial resetting of >1.5 Ga detrital zircons at the time of monazite growth.

Muscovite-bearing pegmatite dikes

Sample JC02-MC-15 is a strongly deformed muscovite-bearing pegmatite dike intruding garnet-staurolite-kyanite schists above the MSF (unit Ycl, Fig. 2). This sample yielded zircons with very dark CL, corresponding to very high U contents (up to 13,000 ppm, Table 4). Analyses of 15 grains cluster around 86 Ma (Fig. 9C), with some spread that we attribute to variable degrees of Pb-loss enhanced by radiation damage following crystallization from a melt at ca. 86 Ma.

Two-Mica Leucogranites

U-Pb zircon ages were obtained from samples ELM91-MSG (Figs. 8A and 9A; Table 4) and JM-DV4 (Figs. 8B and 9B; Table 4), both weakly-deformed two-mica leucogranites that intrude and cross-cut high-grade gneisses of unit Xmi (Fig. 2). Both samples contain two distinct zircon populations. Each sample consists predominantly (>90%) of moderately rounded zircons, (dark CL in sample ELM91-MSG; bright CL in sample JM-DV4; Fig. 8A, B). Analyses of these zircons give a spread of old (~1.5 to 1.7 Ga) $^{207}Pb/^{206}Pb$ ages (Table 4; Fig. 9A, B). A small percentage of each sample (<10%) consists of euhedral zircons or thin rims (bright CL in sample ELM91-MSG, dark CL in sample JM-DV4; Fig. 8A, B). Analyses of these populations are near-concordant, showing minor inheritance and mixing with common-Pb, and yield lower intercept ages of 62.3 ± 2.6 Ma (sample ELM91-MSG, Fig. 9A) and 61.7 ± 4.7 Ma (sample JM-DV4, Fig. 9B). We interpret these ages, identical within uncertainty, to represent crystallization from a leucogranitic melt that inherited older detrital grains derived from partial melting of either Precambrian metasediments or the underlying basement.

DISCUSSION

Timing of Mesozoic metamorphism

We regard the Th/Pb monazite age of 91.5 ± 1.4 Ma from kyanite-garnet mica schist sample MCGM-12 (structurally between the BCD and MSF; Fig. 11) to best

constrain the timing of peak metamorphism at ca. 620 to 680°C and 7 to 9 kbar.

Metamorphic monazite in pelitic rocks first grows in the amphibolite-facies (500 to

650°C, dependent on bulk rock composition: Overstreet, 1967; Smith and Barreiro,

1990; Kingsbury et al., 1993; Ferry, 2000; Foster and Parrish, 2003). Monazite in the

dated sample MCGM-12 is present both in the groundmass and as inclusions in kyanite

porphyroblasts, but was not observed as inclusions in garnet or staurolite, suggesting that

metamorphic monazite grew after staurolite, but before or during the growth of kyanite.

Analyzed monazite grains appear to belong to a single population (Fig. 10A), suggesting

they record a single stage of growth.

The complex BSE patterns and 88 to 75 Ma spread in ages of monazite grains

from leucosome JM-DV3 may reflect prograde metamorphic growth of monazite at

approximately the same time as in MCGM-12, followed protracted monazite growth

during continued metamorphism, resorption during partial melting, and additional growth

during cooling and melt crystallization (e.g., Kohn et al., 2005). Coarse mineral textures

suggest that heating outlasted deformation in the leucosome-rich units, and the presence

of sillimanite suggests that migmatization occurred during decompression and/or heating

into the sillimanite stability field. The similarity of leucosome monazite ages to zircon

ages from pegmatite dikes (sample JC02-MC-15, this study; Applegate et al., 1992;

Applegate, 1994) is consistent with partial melting of metapelite as a source for the

pegmatite dikes. Peak pressure-temperature estimates (Table 3; Fig. 6) overlap the field

of muscovite-pelite wet melting (Thompson and Tracy, 1979), indicating that conditions

were appropriate for the generation of small volumes of partial melt. The age of the

pegmatites may thus record when the most deeply exposed rocks reached their peak

temperature. The time lag between prograde monazite growth near the kyanite isograd at 92 Ma, and pegmatite formation during the thermal maximum at 86 Ma implied by this interpretation is compatible with heating rates inferred from modeling and natural observations (e.g., England and Thompson, 1984; Christensen et al., 1989; Harris et al., 2000). It is unclear if the difference between the 86 Ma pegmatite age determined in this study and the 72 to 64 Ma pegmatite ages determined by Applegate et al. (1992) and Applegate (1994) represents a true age range of crystallization, or if the age difference reflects analytical difficulties related to multi-grain TIMS analysis of zircons affected by both inheritance and radiation-damage induced Pb-loss.

Metamorphism at ca. 92 Ma, and continuing in a protracted fashion at greater depths, suggests that thrust loading related to Early to middle Cretaceous faults of the Sevier belt (Snow and Wernicke, 2000; DeCelles, 2004) may have produced structural-burial related metamorphism. Hoisch and Simpson (1993) suggested that the Last Chance thrust and equivalents, active in Permian or earliest Triassic (Snow et al., 1991; Snow, 1992; Snow and Wernicke, 2000), may have been responsible for burial metamorphism, but these structures are too old to have caused the observed and dated Late Cretaceous metamorphism. Combined data from the southern portion of the Sevier belt suggests that deformation initiated prior to 142 Ma (Walker et al., 1995) and accommodated several 10s of km of shortening during the middle to Late Cretaceous (Snow and Wernicke, 2000; DeCelles, 2004), and thrust faulting ceased before latest Cretaceous time (Burchfiel et al., 1992; DeCelles, 2004). This timing is compatible with a protracted deformational and metamorphic event west of the thrust belt (e.g., England and Thompson, 1984). Labotka and Albee (1988) suggested that heat from the Sierra

Nevada batholith may have contributed to the metamorphism in the Death Valley region. The proximity of the Funeral Mountains to the Sierran batholith prior to Tertiary extension (Snow and Wernicke, 2000), permits a modest thermal contribution from the batholith (e.g., Barton and Hanson, 1989). Our geochronologic constraints on metamorphism and magmatism in the Funeral Mountains overlap the 98 to 86 Ma period of extremely voluminous magmatism in the Sierran batholith (Coleman and Glazner, 1997), which supports the suggestion of Labotka and Albee (1988).

The ca. 62 Ma two-mica leucogranites clearly represent a younger melting episode than the older pegmatite dikes. The abundance of inherited Precambrian grains suggests derivation from partial melting of Precambrian metasediments or underlying basement, and suggests that the 1.7 Ga age from a multi-grain zircon analysis reported by Wright and Troxel (1993) from a similar two-mica granitic dike represents inheritance, as concluded by Applegate and Hodges (1995). Some weakly deformed leucogranite dikes appear to inject normal-sense shear zones. This may indicate early extension at ca. 62 Ma, but it is also possible that the extension is younger, and localized along the dikes due to the mechanical contrast between rock types and their orientation. This second episode of melting, 30 m.y. after peak metamorphism, may be related to extension and decompression, or possibly introduction of additional water into the lower crust from the flat Laramide subducting slab (e.g., Dumitru et al., 1990; Usui et al., 2003). A third possibility is that the granites represent the last melts generated by the relaxation of isotherms within thickened crust after thrusting ceased in latest Cretaceous time (Burchfiel et al., 1992; DeCelles, 2004). Similar-age leucogranites reported from the Death Valley region in the nearby Black Mountains (Miller and Friedman, 1999), and the

Panamint Mountains (Mahood et al., 1996) suggest that the mechanism responsible for latest Cretaceous to earliest Tertiary magmatism was not restricted to the northern Funeral Mountains.

Metamorphism and slip on the Monarch Spring fault

As noted previously, rocks below the MSF are characterized by an abundance of cross-cutting granitic dikes, abundant biotite and hornblende, the presence of sillimanite and migmatites, and the conspicuous lack of mylonitic fabrics. They thus appear to record a different metamorphic and deformational history from rocks above the MSF, which lack migmatization and are overprinted by greenschist-facies alteration and mylonitic deformation.

Thermobarometry indicates that garnet amphibolites above and below the MSF record the same pressures and temperatures within uncertainty, indicating that structural omission across the MSF is less than the 3 to 5 km uncertainty in pressure estimation. This difference in depth, coupled with an unknown amount of lateral displacement, may be enough to explain the difference in metamorphic and deformational history above and below the MSF. Granitic dikes are most abundant near Monarch Canyon, decrease in abundance to the southeast, and are absent beyond Chloride Cliff 6 km to the southeast (Fig. 1; Hoisch and Simpson, 1993), which suggests that rocks above and below the MSF were not separated by a great distance.

Timing of ductile extensional deformation

Younger (ca. 62 Ma), finer-grained two-mica granites intrude and cross-cut gneissic fabrics in the lower plate of the MSF (unit Xmi, Figs. 2 and 4C), but above the MSF, dikes are coarse-grained and moderately to strongly deformed by mylonitic fabrics (Fig. 4D). The contrast in deformational style above and below the MSF may be related to strain partitioning, where strain was mostly accommodated in the weaker marble, pelitic-, and calc-schist above the MSF, leaving the stronger, hornblende- and plagioclase-dominated gneisses below the MSF relatively undeformed.

Based on the field relationships and ages established in previous sections, the formation of mylonite is constrained to be younger than pegmatite dikes dated at ca. 86 Ma, and older than poorly-dated mafic dikes (ca. 22 Ma, Data Repository item) that cross-cut mylonitic fabrics at all levels of Monarch Canyon. We thus follow Hoisch and Simpson (1993) and infer a mid-Tertiary age for the main phase of mylonite development associated with extensional deformation and unroofing. As noted above, limited extension may be as old as 62 Ma, but we find no evidence for the significant episode of Late Cretaceous extension proposed by Applegate and Hodges (1995).

APPENDICES

Appendix A: Electron microprobe analytical procedures

Mineral chemistry was determined with an automated JEOL 733A electron microprobe at Stanford University with operating conditions of 15 nA beam current, and 15 keV accelerating potential, calibrated on natural mineral standards. Raw counts were collected for 20 s and converted to oxide wt% by the CITZAF correction procedure. Minerals were analyzed with a focused (<2µm) beam, except micas, for which a 10µm spot was used.

Appendix B: U-Pb Geochronology laboratory procedures

High-purity mineral separates were obtained using standard mineral-separation

techniques, including crushing, grinding, Frantz magnetic separation (15º forward slope), and heavy liquids. Zircons were concentrated from the fraction that behaved non-magnetically at 1.8 A with a 5º side slope and sank in MEI with a density of ~3.3 g/cc. Monazites were concentrated from the fraction that behaved non-magnetically at 0.5 A with a 10º side slope and magnetically at 1.1 A with a 10º side slope. Mineral grains were hand-picked under a binocular microscope and mounted in epoxy for polishing and gold-coating.

Monazites were analyzed with standard WEN-1 (Stanford-USGS SHRIMP-RG Laboratory monazite age standard 301 Ma). Zircons were analyzed relative to standard R33 (Stanford-USGS SHRIMP-RG Laboratory zircon age standard 419 Ma, Black et al., 2004). Prior to SHRIMP-RG analysis, grains were imaged using cathodoluminescence (CL) for zircon, and back-scattered electron (BSE) images for monazite, to asses any internal zonation. Analyses were performed using a ~5 nA O_2^- primary beam focused to ca. 30 um, and data were reduced using the programs Squid and Isoplot (Ludwig, 2001; 2003).

REFERENCES CITED

Applegate, J. D. R., Walker, J. D., and Hodges, K. V., 1992, Late Cretaceous extensional unroofing in the Funeral Mountains metamorphic core complex, California: Geology, v. 20, p. 519-522.

Applegate, J. D. R., 1994, The unroofing history of the Funeral Mountains metamorphic

core complex, California [Ph.D. thesis]: Massachusetts Institute of Technology, 241 p.

Applegate, J. D. R., and Hodges, K. V., 1995, Mesozoic and Cenozoic extension recorded by metamorphic rocks in the Funeral Mountains, California: Geological Society of America Bulletin, v. 107, no. 9, p. 1063-1076.

Black, L. P., Kamo, S. L., Allen, C. M., Davis, D. W., Aleinikoff, J. N., Valley, J. W., Mundil, R., Campbell, I. H., Korsch, R. J., Williams, I. S., and Foudoulis, C., 2004, Improved $^{206}Pb/^{238}U$ microprobe geochronology by the monitoring of a trace-element-related matrix effect; SHRIMP, ID-TIMS, ELA-ICP-MS and oxygen isotope documentation for a series of zircon standards: Chemical Geology, v. 205, p. 115-140.

Burchfiel, B. C., Cowan, D. S., and Davis, G. A., 1992, Tectonic overview of the Cordilleran orogen in the western United States, *in* Burchfiel, B. C., Lipman, P. W., and Zoback, M. L., eds., The Geology of North America, Vol. G-3, The Cordilleran Orogen: Coterminous U.S.: Boulder, Colorado, Geological Society of America, p. 407-479.

Christensen, J. N., Rosenfeld, J. L., and DePaolo, D. J., 1989, Rates of tectonometamorphic processes from rubidium and strontium isotopes in garnet: Science, v. 244, no. 4911, p. 1465-1469.

Coleman, D. S., and Glazner, A. F., 1997, The Sierra Crest magmatic event: Rapid formation of juvenile crust during the Late Cretaceous in California: International Geology Review, v. 39, p. 768-787.

DeCelles, P. G., 2004, Late Jurassic to Eocene evolution of the Cordilleran thrust belt and foreland basin system, western U.S.A.: American Journal of Science, v. 304, p.

105-168.

DeWitt, E., Sutter, J. F., Wright, L. A., and Troxel, B. W., 1988, Ar-Ar chronology of
Early Cretaceous regional metamorphism, Funeral Mountains, California - A case
study of excess argon [abs.]: Geological Society of America Abstracts with
Programs, v. 20, p. A16.

Dumitru, T. A., Gans, P. B., Foster, D. A., and Miller, E. L., 1991, Refrigeration of the
western Cordilleran lithosphere during Laramide shallow-angle subduction:
Geology, v. 19, p. 1145-1148.

Ellis, D. J., and Green, D. H., 1979, An experimental study of the effect of Ca upon
garnet-clinopyroxene Fe-Mg exchange equilibria: Contributions to Mineralogy
and Petrology, v. 71, p. 13-22.

England, P. C., and Thompson, A. B., 1984, Pressure-temperature-time paths of regional
metamorphism I. Heat transfer during the evolution of regions of thickened continental
crust: Journal of Petrology, v. 25, no. 4, p. 894-928.

Ferry, J. M., 2000, Patterns of mineral occurrence in metamorphic rocks: American
Mineralogist, v. 85, p. 1573-1588.

Foster, G., and Parrish, R. R., 2003, Metamorphic monazite and the generation of P-T-t paths, *in*
Vance, D., Müller, W., and Villa, I. M., eds., Geochronology: Linking the Isotopic
Record with Petrology and Textures: Geological Society, London, Special Publications,
v. 220, p. 25-47.

Giaramita, M. J., 1984, Structural evolution and metamorphic petrology of the Monarch Canyon
area, northern Funeral Mountains, Death Valley, California [M.S. thesis]: University of
California Davis, 145 p.

Graham, C. M., and Powell, R., 1984, A garnet-hornblende geothermometer: calibration, testing, and application to the Pelona Schist, Southern California: Journal of Metamorphic Geology, v. 2, p. 13-31.

Grove, M., Jacobson, C. E., Barth, A. P., and Vucic, A., 2003, Temporal and spatial trends of Late Cretaceous-early Tertiary underplating of Pelona and related schist beneath southern California and southwestern Arizona, *in* Johnson, S. E., Paterson, S. R., Fletcher, J. M., Girty, G. H., Kimbrough, D. L., and Martín-Barajas, A., eds., Geological Society of America Special Paper 374, Tectonic evolution of northwestern México and the southwestern USA: Boulder, Colorado, Geological Society of America, p. 381-406.

Hamilton, W. B., 1988, Detachment faulting in the Death Valley region, California and Nevada: U.S. Geological Survey Bulletin, v. 1790, p. 51-85.

Harris, N., Vance, D., and Ayres, M., 2000, From sediment to granite: timescales of anatexis in the upper crust: Chemical Geology, v. 162, no. 2, p. 155-167.

Hodges, K. V., and Walker, J. D., 1990, Petrologic constraints on the unroofing history of the Funeral Mountain metamorphic core complex, California: Journal of Geophysical Research, v. 95, no. B6, p. 8437-8445.

Hodges, K. V., and Walker, J. D., 1992, Extension in the Cretaceous Sevier orogen, North American Cordillera: Geological Society of America Bulletin, v. 104, p. 560-569.

Hoisch, T. D., 1991, Equilibria within the mineral assemblage quartz + muscovite + biotite + garnet + plagioclase, and implications for the mixing properties of octahedrally-coordinated cations in muscovite and biotite: Contributions to

Mineralogy and Petrology, v. 108, p. 43-54.

Hoisch, T.D., 2000, Conditions of metamorphism in lower plate rocks at Bare Mountain

Nevada: Implications for extensional faulting, in Geological and Geophysical

Characterization Studies of Yucca Mountain, Nevada, A Potential High-Level

Radioactive-Waste Repository: U.S. Geological Survey Digital Data Series 058,

CD-ROM Chapter B

Hoisch, T. D., and Simpson, C., 1993, Rise and tilt of metamorphic rocks in the lower

plate of a detachment fault in the Funeral Mountains, Death Valley, California:

Journal of Geophysical Research, v. 98, no. B4, p. 6805-6827.

Hoisch, T. D., Heizler, M. T., and Zartman, R. E., 1997, Timing of detachment faulting in the

Bullfrog Hills and Bare Mountain area, southwest Nevada: Inferences from $^{40}Ar/^{39}Ar$, K-

Ar, U-Pb, and fission track thermochronology: Journal of Geophysical Research, v. 102,

no. B2, p. 2815-2833.

Holdaway, M. J., and Mukhopadhyay, B., 1993, A reevaluation of the stability relations

of andalusite: Thermochemical data and phase diagram for the aluminum

silicates: American Mineralogist, v. 78, p. 298-315.

Holland, T., and Blundy, J., 1994, Non-ideal interactions in calcic amphiboles and their

bearing on amphibole-plagioclase thermometry: Contributions to Mineralogy and

Petrology, v. 116, p. 433-447.

Holland, T. J. B., and Powell, R., 1998, An internally consistent thermodynamic data set

for phases of petrological interest: Journal of Metamorphic Geology, v. 16, p.

309-343.

Holm, D. K., and Dokka, R. K., 1991, Major late Miocene cooling of the middle crust

associated with extensional orogenesis in the Funeral Mountains, California: Geophysical Research Letters, v. 18, p. 1775-1778.

Ireland, T. R., Wooden, J. L., Persing, H., and Ito, B., 1999, Geological applications and analytical development of the SHRIMP RG [abs.]: Eos Transactions, American Geophysical Union, v. 80, no. 46, p. 1117.

Kingsbury, J. A., Miller, C. F., Wooden, J. L., and Harrison, T. M., 1993, Monazite paragenesis and U-Pb systematics in rocks of the eastern Mojave Desert, California, U.S.A.: implications for thermochronometry: Chemical Geology, v. 110, no. 1-3, p. 147-167.

Kohn, M. J., and Spear, F. S., 1990, Two new geobarometers for garnet amphibolites, with applications to southeastern Vermont: American Mineralogist, v. 75, p. 89-96.

Kohn, M. J., Wieland, M. S., Parkinson, C. D., and Upreti, B. N., 2005, Five generations of monazite in Langtang gneisses: implications for chronology of the Himalayan metamorphic core: Journal of Metamorphic Geology, v. 23, no. 5, p. 399-406.

Kretz, R., 1983, Symbols for rock-forming minerals: American Mineralogist, v. 68, p. 277-279.

Labotka, T. C., 1980, Petrology of a medium-pressure regional metamorphic terrane, Funeral Mountains, California: American Mineralogist, v. 65, p. 670-689.

Labotka, T. C., and Albee, A., 1988, Metamorphism and tectonics of the Death Valley region, California and Nevada, *in* Ernst, W. G., ed., Metamorphism and crustal evolution of the Western United States: Englewood Cliffs, N.J., Prentice-Hall, p. 715-736.

Leake, B. E., Woolley, A. R., Arps, C. E. S., Birch, W. D., Gilbert, M. C., Grice, J. D.,

Hawthorne, F. C., Kato, A., Kisch, H. J., Krivovichev, V. G., Linthout, K., Laird, J., Mandarino, J. A., Maresch, W. V., Nickel, E. H., Rock, N. M. H., Schumacher, J. C., Smith, D. C., Stephenson, N. C. N., Ungaretti, L., Whittaker, E. J. W., and Youzhi, G., 1997, Nomenclature of amphiboles: Report of the Subcommittee on Amphiboles of the International Mineralogical Association, Commission on New Minerals and Mineral Names: American Mineralogist, v. 82, p. 1019-1037.

Ludwig, K. R., 2001, Squid 1.02: A user's manual, Berkeley Geochronology Center Special Publication No. 2.

Ludwig, K. R., 2003, User's manual for Isoplot 3.00: A geochronological toolkit for Microsoft Excel, Berkeley Geochronology Center Special Publication No. 4.

Mahood, G. A., Nibler, G. E., and Halliday, A. N., 1996, Zoning patterns and petrologic processes in peraluminous magma chambers: Hall Canyon pluton, Panamint Mountains, California: Geological Society of America Bulletin, v. 108, no. 4, p. 437-453.

Miller, E. L., and Gans, P. B., 1989, Cretaceous crustal structure and metamorphism in the hinterland of the Sevier thrust belt, western U.S. Cordillera: Geology, v. 17, p. 59-62.

Miller, M. G., and Friedman, R. M., 1999, Early Tertiary magmatism and probable Mesozoic fabrics in the Black Mountains, Death Valley, California: Geology, v. 27, no. 1, p. 19-22.

Overstreet, W. C., 1967, The geologic occurrence of monazite: United States Geological Survey Professional Paper, v. 530, p. 1-327.

Parrish, R. R., 1990, U-Pb dating of monazite and its application to geological problems:

Canadian Journal of Earth Sciences, v. 27, p. 1431-1450.

Pownceby, M. I., Wall, V. J., and O'Neill, H. S. C., 1987, Fe-Mn partitioning between garnet and ilmenite: experimental calibration and applications: Contributions to Mineralogy and Petrology, v. 97, p. 116-126.

Reynolds, M. W., Wright, L. A., and Troxel, B. W., 1986, Geometry and chronology of late Cenozoic detachment faulting, Funeral and Grapevine Mountains, Death Valley, California [abs.]: Geological Society of America Abstracts with Programs, v. 18, no. 2, p. 175.

Smith, H. A., and Barreiro, B., 1990, Monazite U-Pb dating of staurolite grade metamorphism in pelitic schists: Contributions to Mineralogy and Petrology, v. 105, no. 5, p. 602-615.

Snow, J. K., Asmerom, Y., and Lux, D. R., 1991, Permian-Triassic plutonism and tectonics, Death Valley region, California and Nevada: Geology, v. 19, p. 629-632.

Snow, J. K., 1992, Large-magnitude Permian shortening and continental-margin tectonics in the southern Cordillera: Geological Society of America Bulletin, v. 104, p. 80-105.

Snow, J. K., and Wernicke, B. P., 2000, Cenozoic tectonism in the central Basin and Range: Magnitude, rate, and distribution of upper crustal strain: American Journal of Science, v. 300, p. 659-719.

Spear, F. S., 1995, Metamorphic phase equilibria and pressure-temperature-time paths: Washington, D.C., Mineralogical Society of America, 799 p.

Thompson, A. B., and Tracy, R. J., 1979, Model systems for anatexis in pelitic rocks II. Facies series melting and reactions in the system $CaO-KAlO_2-NaAlO_2-Al_2O_3$-

SiO$_2$-H$_2$O: Contributions to Mineralogy and Petrology, v. 70, p. 429-438.

Usui, T., Nakamura, E., Kobayashi, K., Maruyama, S., and Helmstaedt, H., 2003, Fate of the subducted Farallon plate inferred from eclogite xenoliths in the Colorado Plateau: Geology, v. 31, no. 7, p. 589-592.

Walker, J. D., Burchfiel, B. C., and Davis, G. A., 1995, New age controls on initiation and timing of foreland belt thrusting in the Clark Mountains, southern California: Geological Society of America Bulletin, v. 107, no. 6, p. 742-750.

Wasserburg, G. J., Wetherill, G. W., and Wright, L. A., 1959, Ages in the Precambrian terrane of Death Valley, California: Journal of Geology, v. 67, p. 702-708.

Wells, M., and Allmendinger, R. W., 1990, An early episode of pure shear in the upper plate of the Raft River metamorphic core complex, Black Pine Mountains, southern Idaho: Journal of Structural Geology, v. 12, p. 851-867.

Williams, I. S., 1998, U-Th-Pb geochronology by ion microprobe, *in* McKibben, M. A., Shanks, W. C., III, and Ridley, W. I., eds., Applications of microanalytical techniques to understanding mineralizing processes: Reviews in Economic Geology v. 7, Society of Economic Geologists, p. 1-35.

Wright, L. A., and Troxel, B. W., 1993, Geologic map of the central and northern Funeral Mountains and adjacent areas, Death Valley region, southern California, scale 1:48,000: U.S. Geological Survey Miscellaneous Investigations Series, v. I-2305.

FIGURE CAPTIONS

Figure 1: Geologic map of the Funeral Mountains, Death Valley, California, showing location of study area and regional geologic setting. Main map after Hoisch and Simpson (1993) and Labotka (1980). Inset map after Burchfiel et al., (1992).

Figure 2. Detailed geologic map of Monarch Canyon, northern Funeral Mountains, showing rock units, major structures, and sample locations.

Figure 3. Lower hemisphere, equal-area projections of structural data collected near Monarch Canyon.

Figure 4. Field photos of the MSF. (A) View down canyon, to the southwest; arrows mark the MSF. Note that the MSF is approximately parallel to layering above it (unit Ycs), but truncates more steeply-dipping layers beneath (unit Xmi). (B) View to the southwest; arrows mark the MSF. Quartz mylonite beneath the MSF is cut by a mafic dike, which is itself brittley offset. (C) View to the northwest, unit Xmi. Note folded muscovite pegmatite dikes approximately concordant with gneissic foliation cut by finer-grained, less deformed, two-mica leucogranite dikes. View is approximately 15 m high. (D) Boudinaged granitic pegmatite dikes rotated into parallelism with the mylonitic foliation in units Ycm and Ycs. View to the south.

Figure 5. (A) Photomicrograph of quartz mylonite adjacent to the MSF. Mica fish

indicate a top-to-the-NW sense of shear. Plane polarized light. (B) Photomicrograph of

garnet amphibolite MC-E. Note internal foliation defined by inclusion trails in garnet

(highlighted by white line). Crossed polars. (C) Photomicrograph of garnet-sillimanite

gneiss MCGM-9. Plane polarized light. (D) Backscattered electron image of garnet

amphibolite MC-E. The line marks the location of the compositional profile shown in

Fig. 6A. Image brightness is proportional to average atomic number. (E) Backscattered

electron image of tonalitic gneiss MCGM-5. The line marks the location of the

compositional profile shown in Fig. 6D. Image brightness is proportional to average

atomic number.

Figure 6. Garnet zoning profiles. (A) sample MC-E (above the MSF, profile location

shown in Fig. 5D). (B) sample MCGM-8B (below the MSF). (C) sample MCGM-1B

(below the MSF). (D) sample MCGM-5 (below the MSF, profile location shown in Fig.

5E). Note expanded distance scale for sample MCGM-5.

Figure 7. Pressure-temperature estimates for Monarch Canyon samples.

THERMOCALC estimates are shown as 1σ uncertainty ellipses, and squares indicate the

intersection of the Graham and Powell (1984) thermometer with the Kohn and Spear

(1990) barometers. Open squares represent analyses outside the calibration range (see

text). Key to numbered reactions: (1) Ms + Ab + Kfs + Qtz + H_2O = melt; (2) Ms + Kfs

+ Qtz + H_2O = melt; (3) Ms + Ab + Qtz = Kfs + Al_2SiO_5 + melt; (4) Ms + Qtz = Kfs +

Al_2SiO_5 + melt. Reactions 1-4, and the fields for dry and wet melting of Ms-pelite

(stippled) are from Thompson and Tracy (1979), and the aluminosilicate diagram is from Holdaway and Mukhopadhyay (1993).

Figure 8. Images of grains used for SHRIMP-RG geochronology showing locations of individual spot analyses. Cathodoluminescence images of zircons from leucogranites ELM91-MSG (A) and JM-DV4 (B) with corresponding U-Pb ages. Backscattered electron images of monazites from garnet-kyanite-staurolite schist MCGM-12 (C) and leucosomal segregation JM-DV3 (D) with corresponding Th-Pb ages. All ages are in millions of years ± 1σ. Complete sample information is listed in table 4.

Figure 9. Terra-Wasserburg concordia diagrams for zircon analyses; error ellipses are 2σ. (A) leucogranite MSG. (B) leucogranite dike JM-DV4. (C) pegmatite dike JC02-MC-15.

Figure 10. Terra-Wasserburg concordia diagrams for monazite analyses; error ellipses are 2σ. (A) garnet-kyanite-staurolite schist MCGM-12. (B) leucosomal segregation JM-DV3.

Figure 11. Schematic cross-section through Monarch Canyon showing major lithologies, structures, and relative structural position of samples discussed in this study.

117° 00'
116° 45'
36° 45'

Fig. 2

kyanite zone

Monarch Canyon

BOUNDARY CANYON DETACHMENT

Chloride Cliff ▲

staurolite zone

bio + Ky

BCD slip direction

KEANE

garnet zone

Quaternary deposits

Tertiary rocks

Proterozoic & Cambrian sedimentary rocks

Proterozoic metamorphic rocks

WONDER

FAULT

garnet

Mesozoic granitic plutons

Pz - Mz allochthons

Cordilleran Miogeocline

Sevier Thrust Belt

Study Area

36° 30'

MC-Fig1.ai
Mattinson, Colgan, Metcalf, Miller, and Wooden
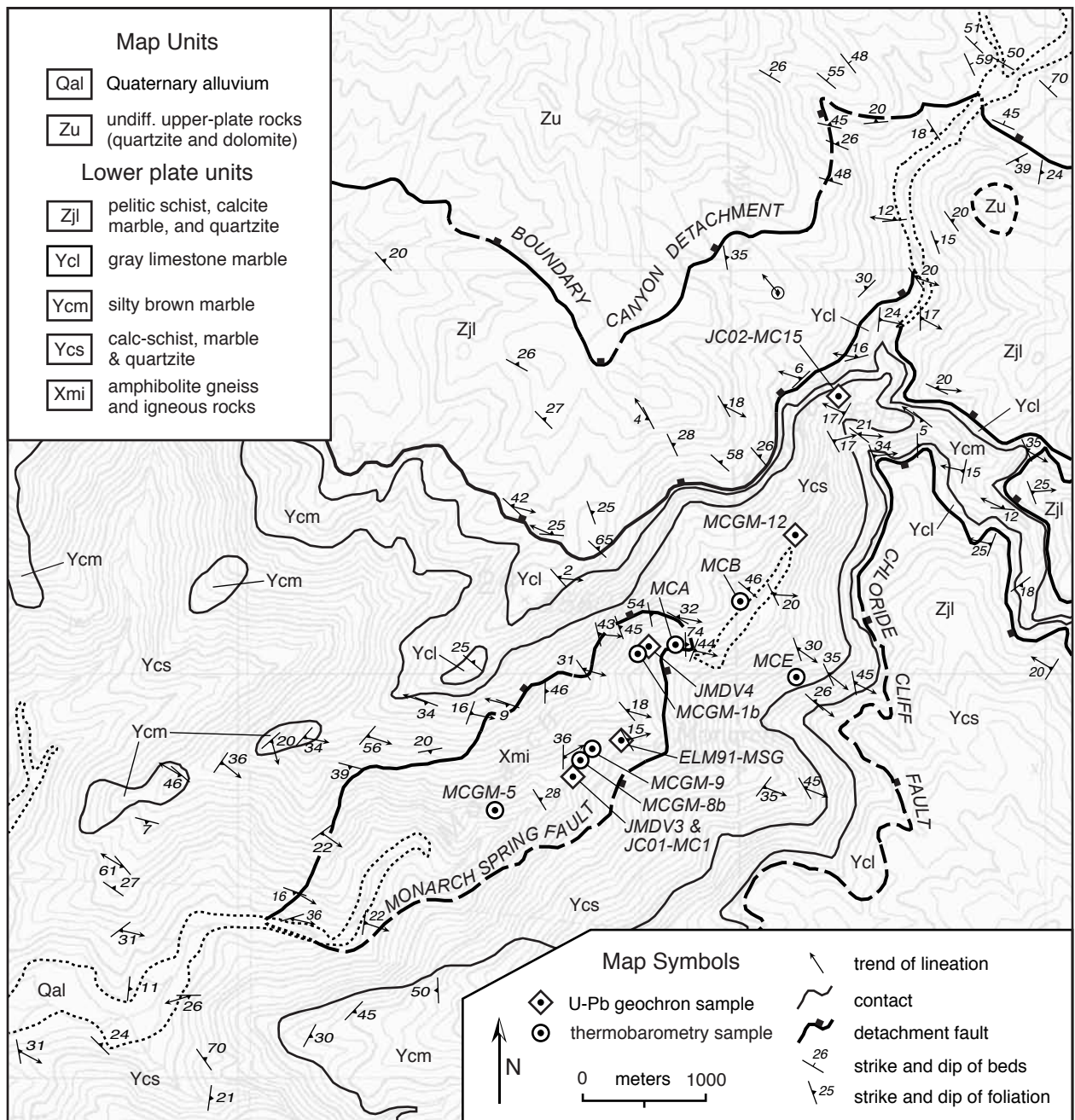
MC-Fig2.ai
Mattinson, Colgan, Metcalf, Miller, and Wooden

Foliation   Amphibolite facies   Lineation
                  (below MSF)

Foliation   Mylonite   Lineation
               (above MSF)

BCD
corrugations
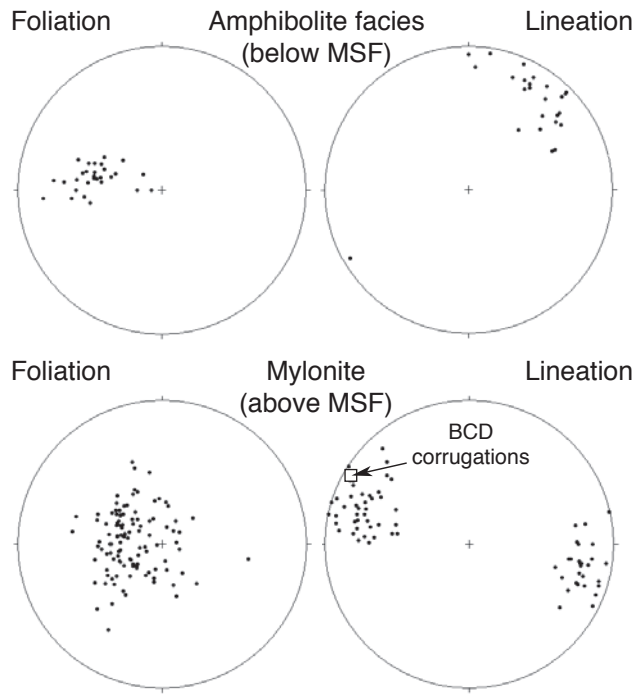
MC-Fig3.ai
Mattinson, Colgan, Metcalf, Miller, and Wooden

A

B

Qtz
mylonite

mafic
dike

C

D
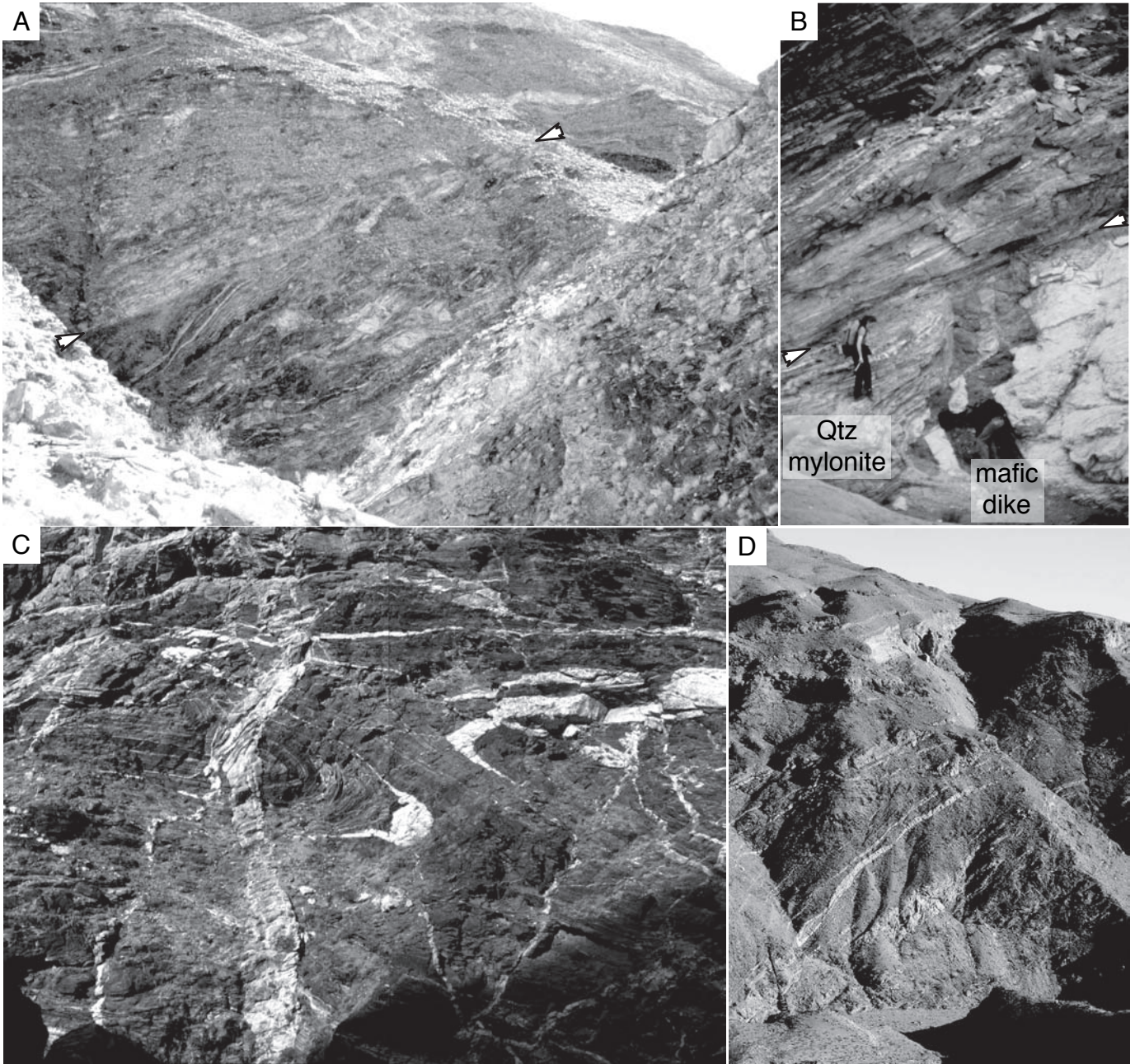
MC-Fig4.ai
Mattinson, Colgan, Metcalf, Miller, and Wooden

A

SE   NW

Qtz

Ms

0.5 mm

B

Hbl + Qtz + Pl

Grt

5 mm

C

Grt

Qtz + Pl   Sil

Bt + Ms

5 mm

D

Hbl

Qtz

Grt

1 mm

E

Qtz   Hbl

Pl   Bt

Grt

Ep

100 μm
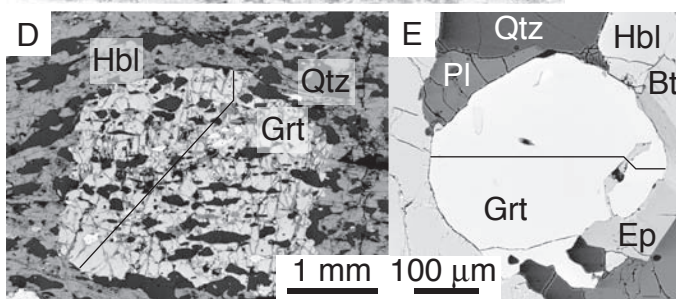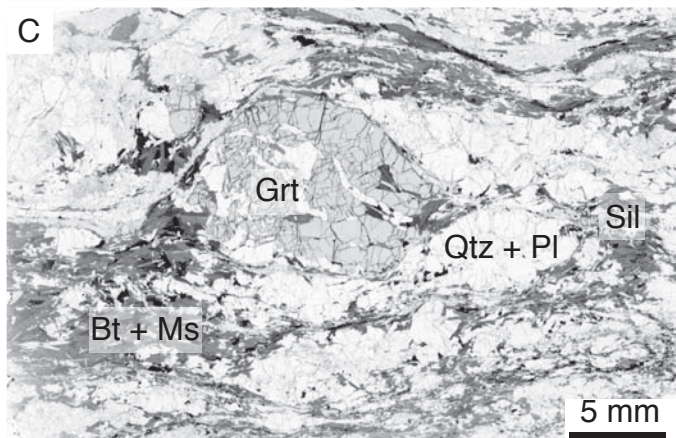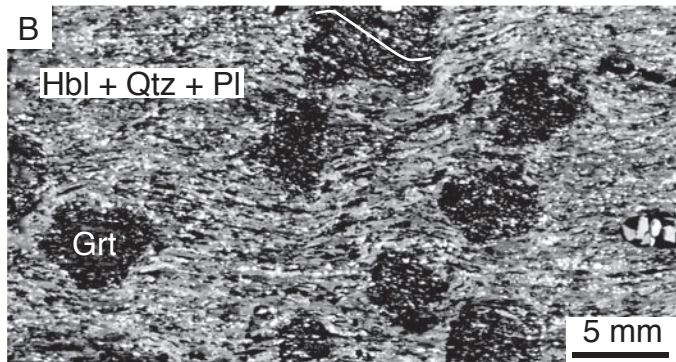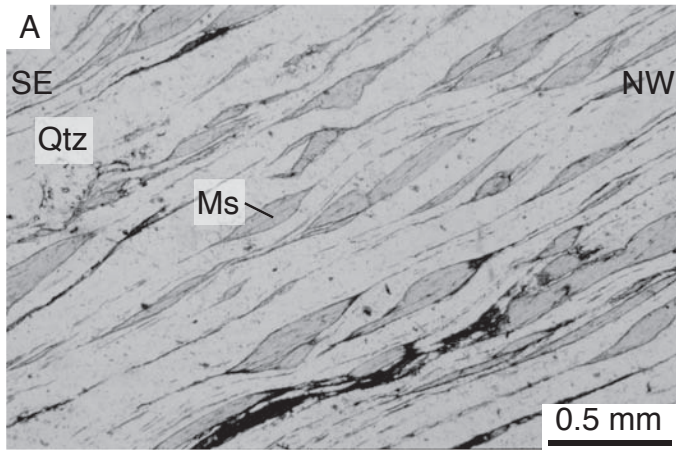
MC-Fig5.ai
Mattinson, Colgan, Metcalf, Miller, and Wooden

A.

MC-E

B.

MCGM-8B

C. MCGM-1B

D. MCGM-5

Distance (μm)
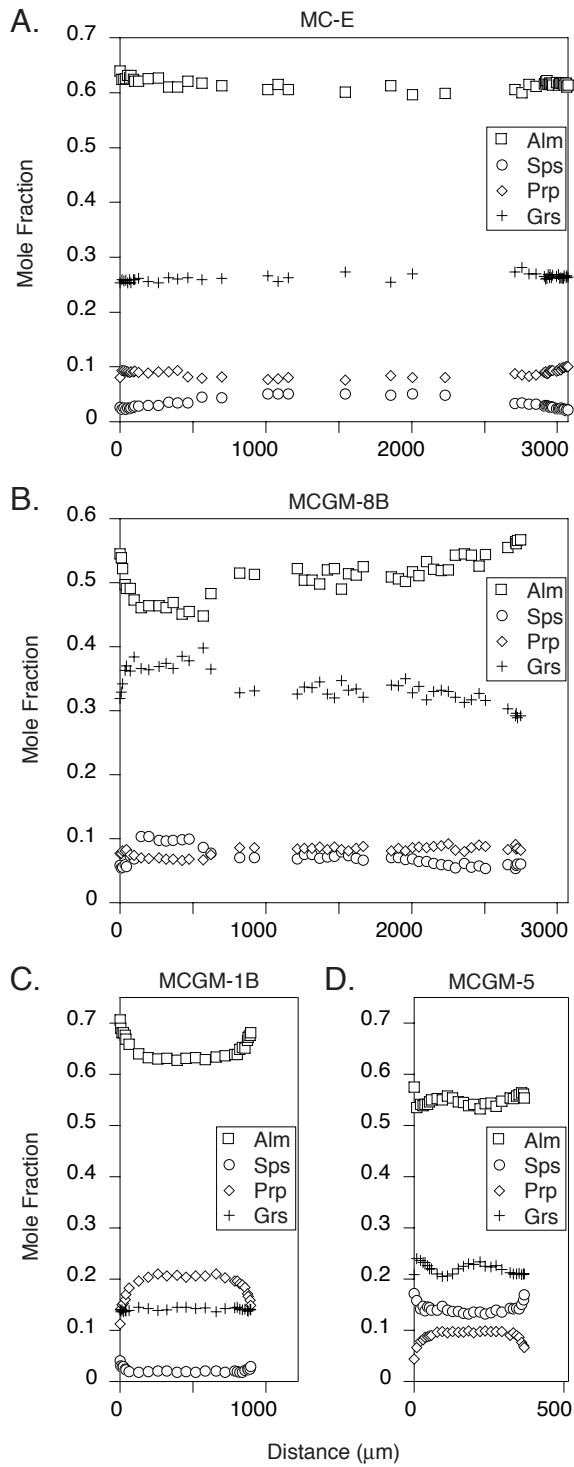
MC-Fig6.ai
Mattinson, Colgan, Metcalf, Miller, and Wooden
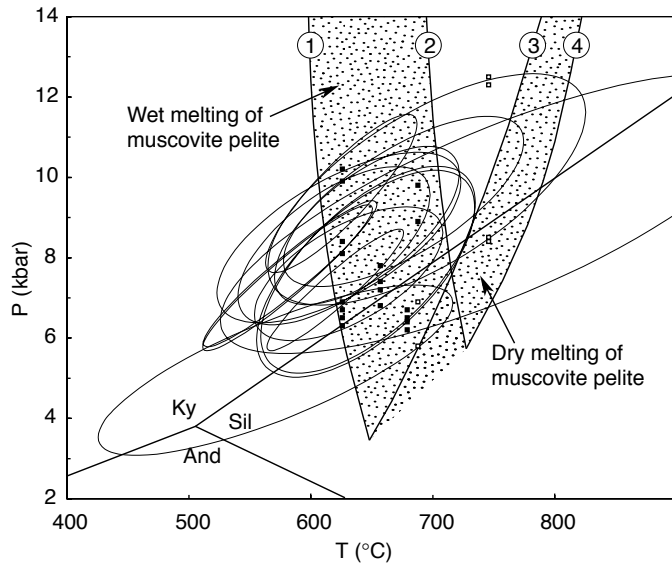
MC-Fig7.ai
Mattinson, Colgan, Metcalf, Miller, and Wooden

A

1660.2 ± 18.9
64.7 ± 1.3
1720.7 ± 19.9

100μm

B

1167.0 ± 6.6
1530.8 ± 9.3
53.0 ± 0.3
64.4 ± 0.3
1181.0 ± 11.2

15kV   X70   200μm

C

MCGM12-1
94 ± 1 Ma

100μm

D

DV3-6
75 ± 1 Ma

15kV   X550   20μm   20 38 BEC
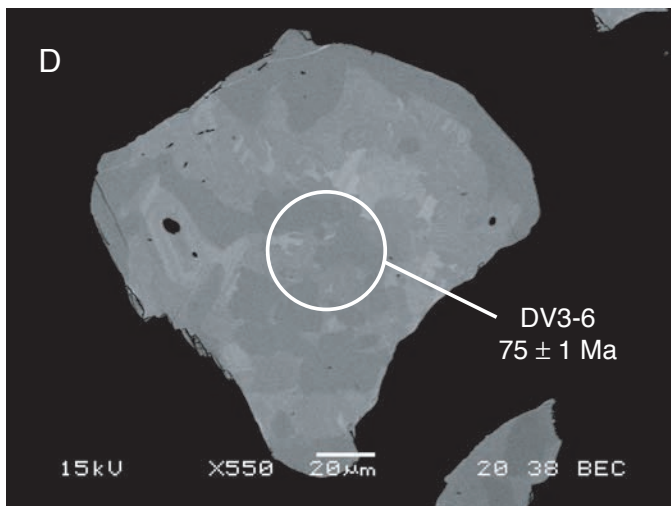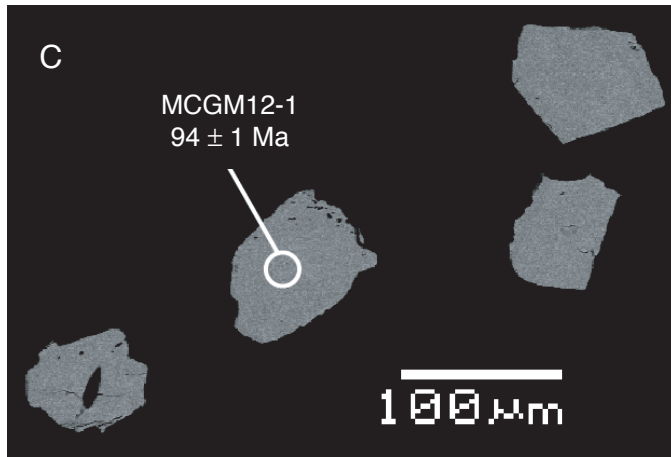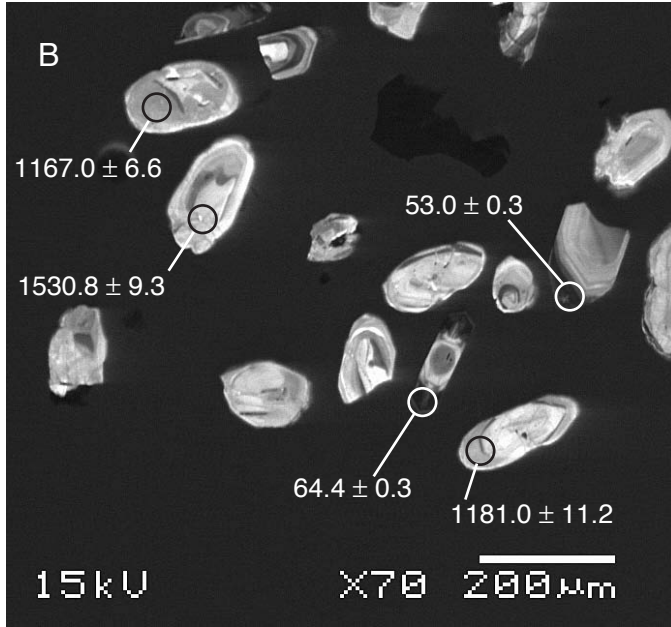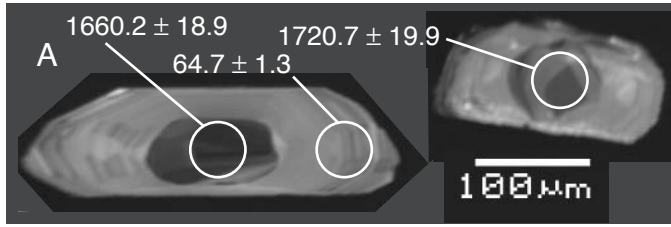
MC-Fig8.ai
Mattinson, Colgan, Metcalf, Miller, and Wooden

A.
ELM91-MSG leucogranite
Intercepts at 62.3 ± 2.6 &
4507 ± 2600 Ma,
MSWD = 0.97

B.
JM-DV-4 leucogranite dike
Intercepts at 61.7 ± 4.7 &
2367 ± 1100 Ma,
MSWD = 4.3

C.
JC02-MC-15 pegmatite dike
Intercepts at 85.8 ± 1.4 &
3837 ± 1500 Ma
MSWD = 1.5
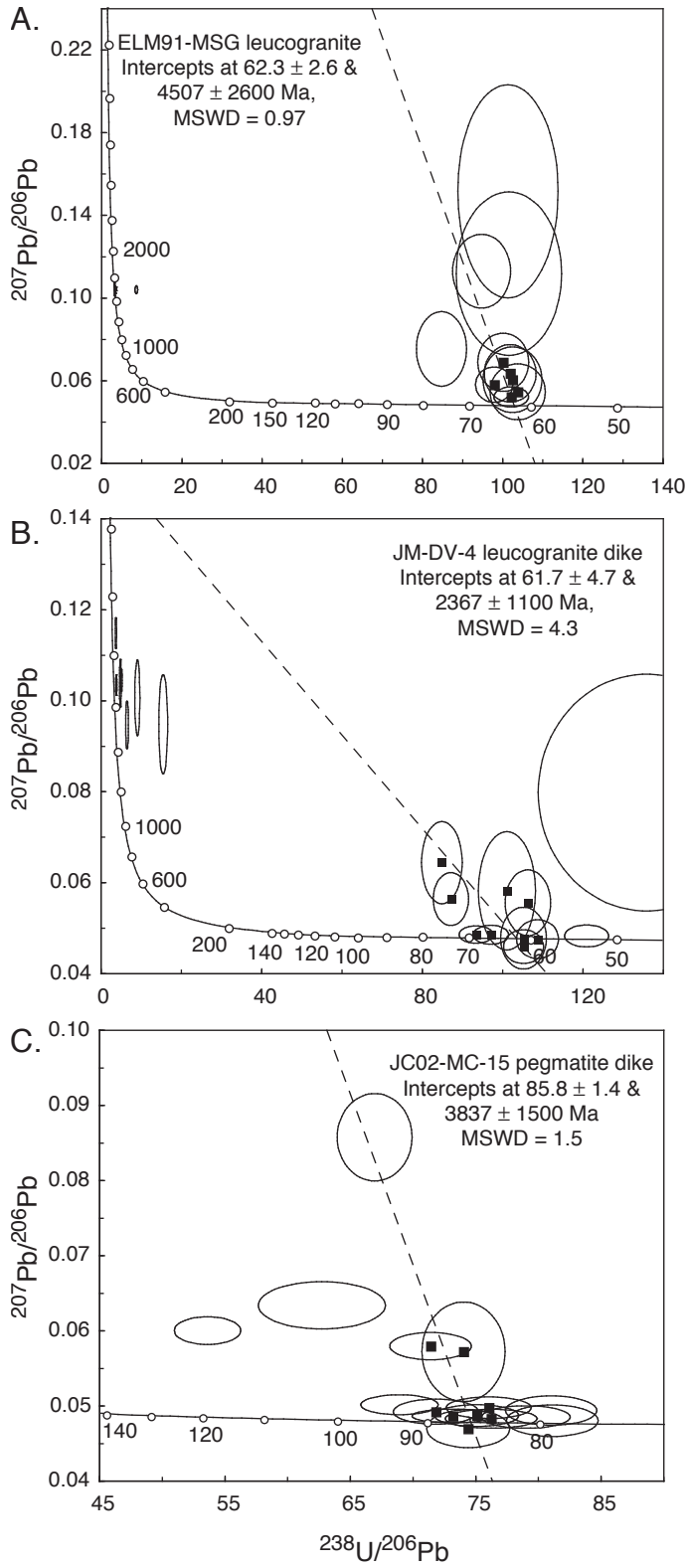
MC-Fig9.ai
Mattinson, Colgan, Metcalf, Miller, and Wooden

A. MCGM-12 Ky-schist
Intercepts at 93.8 ± 1 &
5010 ± 6200 Ma MSWD = 3.0
Weighted mean Th/Pb age
91.5 ± 1.4 Ma, MSWD = 3.6

B. JM-DV-3 leucosome
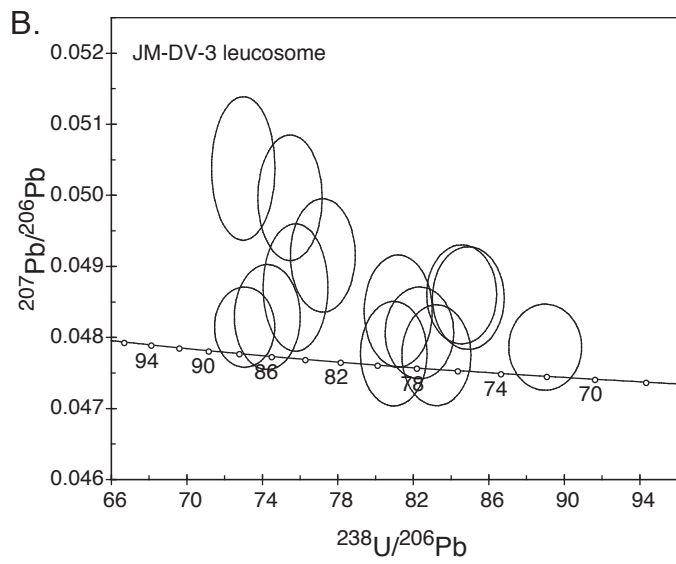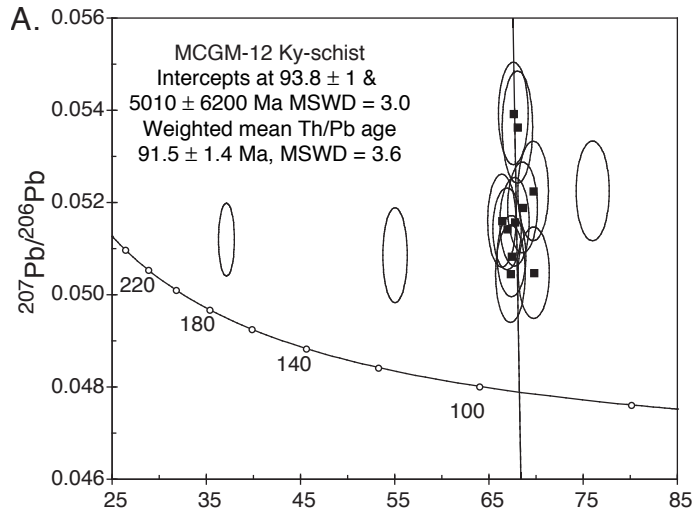
MC-Fig10.ai
Mattinson, Colgan, Metcalf, Miller, and Wooden

SW / NE

Scale: 0 — meters — 1000
VE approx. 2X

Labels in figure:
- Proterozoic sedimentary rocks
- amphibolite boudins
- marble mylonites
- BCD
- 86 Ma pegmatite
- Zu
- CCF
- 22 Ma mafic dike
- Zjl
- quartz mylonites
- Ycl
- sandstone boudins
- 90–70 Ma leucosomes in high-grade gneiss
- MSF
- Ycm
- kyanite schists 92 Ma
- 62 Ma leucogranites
- Ycs
- 7-9 kbar 620-680°C
- Xmi
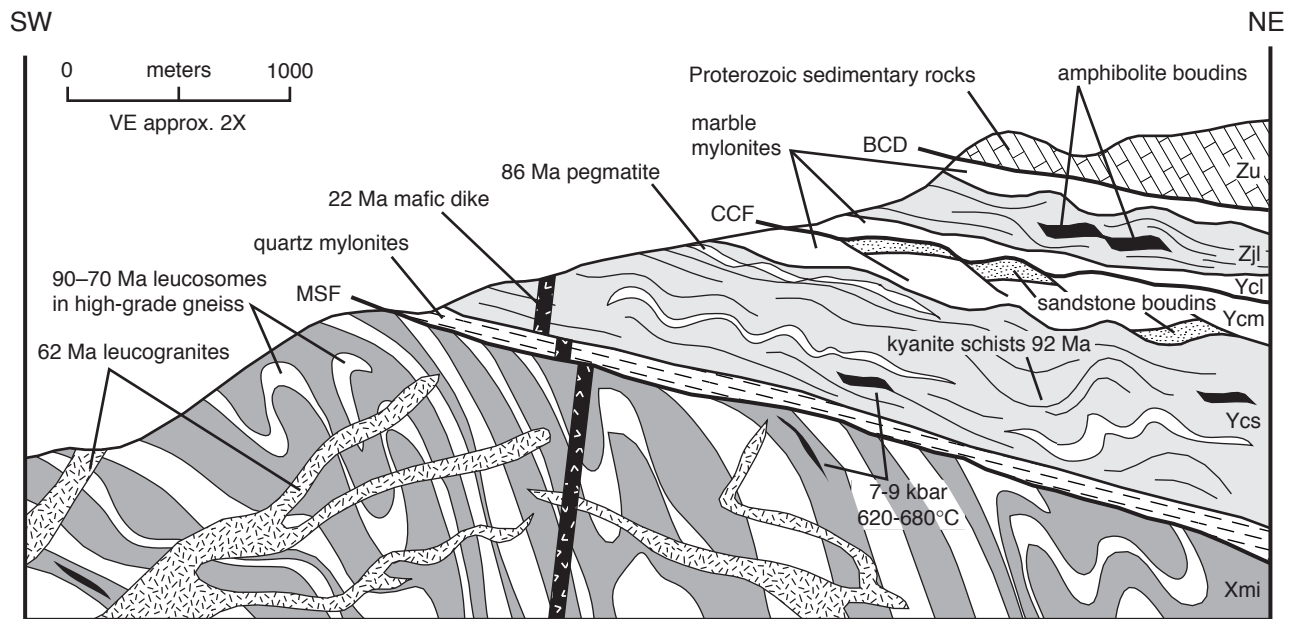
MC-Fig11.ai
Mattinson, Colgan, Metcalf, Miller, and Wooden

TABLE 1. LOCATIONS AND PARAGENESES OF THERMOBAROMETRY AND GEOCHRONOLOGY SAMPLES

Sample	Lat (N)	Long (W)	Grt	St	Ky	Sil	Ep	Hbl	Bt	Ms	Pl	Kfs	Qtz	Accessory
MC-E	36°43.404'	116°55.063'	x					x			x		x	Spn, opq
MC-B	36°43.505'	116°55.174'	x					x			x		x	Spn, opq
MC-A	36°43.445'	116°55.281'	x				x	x			x		x	Spn, opq
MCGM-1B	36°43.423'	116°55.367'	x				x	x	x		x		x	Ilm, Zrn
MCGM-9	36°43.295'	116°55.440'	x			x			x	x	x		x	Zrn
MCGM-8B	36°43.283'	116°55.451'	x				x	x	x		x		x	Ap, opq
MCGM-5	36°43.217'	116°55.599'	x				x	x	x	x	x		x	Mag, Ilm, Ap, Zrn
JC02-MC15	36°43.778'	116°55.020'								x	x	x	x	Ap, Zrn
MCGM-12	36°43.581'	116°55.079'	x	x	x				x	x	x		x	Ap, Zrn, Mnz, Xen
JM-DV-4	36°43.431'	116°55.360'							x	x	x	x	x	Ap, Zrn
ELM91-MSG	36°43.314'	116°55.539'							x	x	x	x	x	Ap, Zrn
JM-DV-3	36°43.290'	116°55.448'									x	x	x	Zrn, Mnz
JC01-MC1	36°43.290'	116°55.448'	x			x			x		x	x	x	Ap, Zrn, Mnz

Note: mineral abbreviations after Kretz (1983) except Xen (xenotime), and opq (opaque, undifferentiated).

TABLE 2. MINERAL COMPOSITIONS USED FOR THERMOBAROMETRY

Sample	MC-E	MC-B	MC-A	MCGM-1B	MCGM-9	MCGM-9	MCGM-8B	MCGM-5	MCGM-5	MCGM-8B	MCGM-5
Analysis	g 571	g 615	g 371	g 291	g 695	g 710	g 426	g 400	g 437	ep 373	ep 466
Mineral	Grt	Grt	Grt	Grt	Grt (edge)	Grt (rim)	Grt	Grt	Grt	Ep	Ep
SiO_2	38.18	38.64	38.47	37.59	36.96	37.38	37.58	36.82	36.97	39.24	37.54
TiO_2	0.07	0.04	0.08	0.00	0.00	0.01	0.00	0.00	0.31	0.21	0.10
Al_2O_3	20.17	20.67	21.25	21.75	20.44	21.29	21.22	20.07	20.76	29.39	24.83
Cr_2O_3	0.02	0.06	0.06	0.06	0.00	0.02	0.00	0.00	0.00	0.02	0.00
Fe_2O_3	0.53	0.00	0.00	1.04	0.00	0.11	0.48	1.89	0.90	5.45	12.06
FeO	28.19	28.69	22.38	28.68	34.34	32.92	25.26	23.05	24.22	0.00	0.00
MnO	1.11	0.52	2.08	0.91	3.72	3.48	2.68	6.42	8.07	0.04	0.36
MgO	2.46	3.42	1.83	5.03	2.36	3.72	2.09	2.02	1.25	0.05	0.04
CaO	9.34	8.17	14.06	4.97	1.07	1.18	10.32	8.44	7.69	23.55	22.96
Na_2O	0.01	0.00	0.01	0.00	0.00	0.02	0.00	0.01	0.00	0.00	0.00
K_2O	0.00	0.00	0.01	0.00	0.01	0.00	0.00	0.00	0.00	0.00	0.00
Totals	100.08	100.20	100.22	100.04	98.91	100.14	99.63	98.73	100.17	97.97	97.91
Oxygens	12.	12.	12.	12.	12.	12.	12.	12.	12.	12.5	12.5
Si	3.035	3.046	3.018	2.958	3.025	2.993	2.991	2.984	2.971	3.022	2.975
Ti	0.004	0.002	0.005	0.000	0.000	0.001	0.000	0.000	0.019	0.012	0.006
Al	1.890	1.921	1.965	2.018	1.972	2.009	1.991	1.918	1.967	2.668	2.320
Cr	0.001	0.003	0.003	0.004	0.000	0.001	0.000	0.000	0.000	0.001	0.000
Fe^{3+}	0.031	0.000	0.000	0.062	0.000	0.007	0.029	0.115	0.055	0.316	0.719
Fe^{2+}	1.874	1.891	1.468	1.888	2.351	2.204	1.681	1.563	1.628	0.000	0.000
Mn	0.075	0.034	0.138	0.061	0.258	0.236	0.181	0.441	0.549	0.003	0.024
Mg	0.291	0.401	0.214	0.590	0.288	0.444	0.248	0.245	0.150	0.005	0.004
Ca	0.795	0.690	1.182	0.419	0.094	0.101	0.880	0.733	0.662	1.945	1.952
Na	0.002	0.000	0.001	0.000	0.000	0.004	0.001	0.001	0.001	0.000	0.000
K	0.000	0.000	0.001	0.000	0.001	0.000	0.000	0.000	0.000	0.000	0.000
Sum	8.000	7.990	7.995	8.000	7.990	8.000	8.000	8.000	8.000	7.973	8.000

TABLE 2. MINERAL COMPOSITIONS USED FOR THERMOBAROMETRY (cont.)

Sample	MC-E	MC-B	MC-A	MCGM-1B	MCGM-8B	MCGM-5	MCGM-1B	MCGM-9	MCGM-8B	MCGM-5	MCGM-9	MCGM-5
Analysis	amph 564	amph 614	amph 369	amph 284	amph 332	amph 396	bi 293	bi 670	bi 345	bi 426	mu 686	mu 486
Mineral	Hbl	Hbl	Hbl	Hbl	Hbl	Hbl	Bt	Bt	Bt	Bt	Ms	Ms
SiO_2	43.88	42.76	43.73	41.93	42.26	38.90	36.80	35.56	36.21	34.61	45.79	45.42
TiO_2	0.72	0.74	0.62	0.60	0.73	0.73	1.96	2.03	2.70	0.83	0.40	0.05
Al_2O_3	14.38	15.94	12.82	16.27	15.16	14.89	17.41	18.49	17.04	16.95	34.62	32.41
Cr_2O_3	0.07	0.09	0.11	0.04	0.03	0.00	0.02	0.00	0.00	0.00	0.00	0.00
Fe_2O_3	1.29	1.72	0.56	2.18	0.26	4.91	0.00	0.00	0.00	2.21	0.00	1.30
FeO	15.64	13.35	15.67	14.24	16.82	17.61	17.48	20.85	18.89	22.00	1.96	2.68
MnO	0.15	0.09	0.16	0.04	0.18	0.47	0.01	0.14	0.13	0.29	0.00	0.00
MgO	8.07	8.89	8.98	8.08	7.59	5.77	10.83	8.57	10.38	8.18	1.06	0.99
CaO	11.34	11.11	11.70	10.79	11.72	10.99	0.01	0.00	0.00	0.13	0.00	0.02
Na_2O	1.15	1.44	1.28	1.62	1.15	1.71	0.17	0.11	0.07	0.04	0.45	0.61
K_2O	0.38	0.50	0.79	0.51	1.35	1.26	9.19	9.59	9.69	9.22	10.91	10.40
Totals	97.07	96.64	96.43	96.29	97.24	97.23	93.87	95.35	95.12	94.46	95.20	93.89
Oxygens	23.	23.	23.	23.	23.	23.	11.	11.	11.	11.	11.	11.
Si	6.530	6.346	6.585	6.284	6.361	6.016	2.808	2.727	2.761	2.723	3.071	3.110
Ti	0.080	0.082	0.071	0.067	0.083	0.085	0.112	0.117	0.155	0.049	0.020	0.003
Al	2.523	2.789	2.276	2.875	2.690	2.715	1.566	1.672	1.532	1.572	2.737	2.616
Cr	0.008	0.011	0.013	0.005	0.003	0.000	0.001	0.000	0.000	0.000	0.000	0.000
Fe^{3+}	0.145	0.192	0.063	0.245	0.029	0.571	0.000	0.000	0.000	0.131	0.000	0.067
Fe^{2+}	1.946	1.657	1.973	1.785	2.117	2.278	1.116	1.337	1.205	1.448	0.110	0.153
Mn	0.018	0.011	0.021	0.005	0.023	0.061	0.001	0.009	0.008	0.019	0.000	0.000
Mg	1.791	1.966	2.016	1.804	1.702	1.329	1.232	0.979	1.180	0.959	0.106	0.101
Ca	1.808	1.767	1.888	1.733	1.890	1.821	0.000	0.000	0.000	0.011	0.000	0.001
Na	0.333	0.414	0.373	0.470	0.335	0.512	0.024	0.017	0.011	0.007	0.058	0.081
K	0.073	0.096	0.152	0.098	0.259	0.249	0.895	0.939	0.944	0.927	0.934	0.909
Sum	15.255	15.331	15.432	15.370	15.493	15.636	7.756	7.797	7.795	7.844	7.037	7.041

TABLE 2. MINERAL COMPOSITIONS USED FOR THERMOBAROMETRY (cont.)

Sample	MC-E	MC-E	MC-B	MC-B	MC-A	MC-A	MCGM-1B	MCGM-1B	MCGM-9	MCGM-8B	MCGM-8B	MCGM-5	MCGM-5	MCGM-5
Analysis	fsp 580	fsp 576	fsp 625	fsp 641	fsp 421	fsp 430	fsp 250	fsp 238	fsp 766	fsp 353	fsp 358	fsp 321	fsp 345	ilhem 431
Mineral	Pl	Pl	Pl	Pl	Pl	Pl	Pl	Pl	Pl	Pl	Pl	Pl	Pl	Ilm
SiO_2	53.83	61.79	52.65	58.30	47.07	58.01	55.96	56.71	63.93	53.93	55.01	56.81	63.26	0.02
TiO_2	0.03	0.04	0.07	0.03	0.03	0.05	0.01	0.01	0.01	0.00	0.03	0.00	0.00	49.76
Al_2O_3	29.61	23.97	29.99	26.69	33.93	26.60	28.24	27.74	22.20	29.97	28.93	27.85	23.38	0.00
Cr_2O_3	0.08	0.04	0.09	0.07	0.07	0.04	0.00	0.03	0.01	0.05	0.03	0.00	0.01	0.00
Fe_2O_3	0.17	0.25	0.09	0.04	0.02	0.08	0.21	0.01	0.02	0.00	0.00	0.01	0.11	5.42
FeO	0.00	0.00	0.00	0.00	0.00	0.00	0.00	0.00	0.00	0.00	0.00	0.00	0.00	41.29
MnO	0.06	0.06	0.05	0.00	0.06	0.00	0.00	0.00	0.02	0.00	0.01	0.00	0.02	3.29
MgO	0.01	0.01	0.01	0.01	0.02	0.00	0.00	0.00	0.00	0.01	0.00	0.00	0.00	0.01
CaO	11.21	4.75	12.87	8.17	16.70	8.30	10.18	9.60	3.01	11.96	11.04	9.17	3.86	0.09
Na_2O	4.89	8.58	4.22	6.87	2.08	6.88	5.80	6.17	9.92	4.57	5.29	6.31	9.40	0.00
K_2O	0.04	0.08	0.04	0.07	0.03	0.10	0.02	0.04	0.13	0.04	0.07	0.05	0.10	0.00
Totals	99.93	99.55	100.08	100.26	100.01	100.08	100.43	100.32	99.24	100.53	100.40	100.19	100.15	99.89
Oxygens	8.	8.	8.	8.	8.	8.	8.	8.	8.	8.	8.	8.	8.	3.
Si	2.430	2.748	2.385	2.599	2.160	2.594	2.506	2.537	2.840	2.421	2.469	2.541	2.791	0.000
Ti	0.001	0.001	0.002	0.001	0.001	0.002	0.000	0.000	0.000	0.000	0.001	0.000	0.000	0.948
Al	1.576	1.257	1.601	1.403	1.836	1.402	1.491	1.463	1.163	1.586	1.531	1.469	1.216	0.000
Cr	0.003	0.002	0.003	0.002	0.003	0.001	0.000	0.001	0.000	0.002	0.001	0.000	0.001	0.000
Fe^{3+}	0.006	0.008	0.003	0.001	0.001	0.003	0.007	0.000	0.001	0.000	0.000	0.000	0.004	0.103
Fe^{2+}	0.000	0.000	0.000	0.000	0.000	0.000	0.000	0.000	0.000	0.000	0.000	0.000	0.000	0.875
Mn	0.002	0.002	0.002	0.000	0.002	0.000	0.000	0.000	0.001	0.000	0.000	0.000	0.001	0.071
Mg	0.001	0.001	0.001	0.001	0.001	0.000	0.000	0.000	0.000	0.001	0.000	0.000	0.000	0.000
Ca	0.542	0.226	0.625	0.390	0.821	0.398	0.488	0.460	0.143	0.575	0.531	0.439	0.183	0.003
Na	0.428	0.740	0.370	0.594	0.185	0.597	0.503	0.535	0.855	0.398	0.460	0.547	0.804	0.000
K	0.002	0.004	0.002	0.004	0.002	0.006	0.001	0.003	0.007	0.003	0.004	0.003	0.005	0.000
Sum	4.992	4.989	4.995	4.996	5.012	5.003	4.997	5.000	5.009	4.985	4.996	4.999	5.004	2.000

Note: Ferric iron estimation uses the AX program of Holland and Powell (1998), which employs the following constraints: garnet (8 cations, 12 oxygens); epidote (all ferric); hornblende (average of maximum and minimum constraints following Holland and Blundy 1994 and Leake et al. 1997); biotite (Tet + Oct = 6.9 for 11 oxygens, max ratio = 0.15); muscovite (Tet + Oct = 6.05 for 11 oxygens, max ratio = 0.7); plagioclase (all ferric); ilmenite (2 cations, 3 oxygens). These calculations are appropriate for THERMOCALC and Holland and Blundy (1994) P-T estimates, but all ferrous iron is used for the Graham and Powell (1982) and Pownceby et al. (1987) thermometers; the Kohn and Spear (1990) barometer uses minimum ferric iron in amphibole using the method of Spear and Kimball (1984) and all ferrous iron in garnet.

TABLE 3. THERMOBAROMETRY RESULTS

| Sample | Note | THERMOCALC | | GP 84 | KS 90 Fe | KS 90 Mg | HB 94 | Assemblage used |
		T±1σ (°C)	P±1σ (kbar)	T (°C)	P (kbar)	P (kbar)	T °C (at P)	for THERMOCALC*
MC-E	an	631±51	7.6±1.1	626	6.9	6.5	634/600 (7)	g, pl, hbl, q
	ab	695±86	9.7±1.9	626	10.2	9.9	616/561 (10)	g, pl, hbl, q
MC-B	an	619±52	8.3±1.3	626	6.7	6.3	637/611 (6.5)	g, pl, hbl, q
	ab	646±50	8.8±1.3	626	8.4	8.1	598/627 (8)	g, pl, hbl, q
MC-A	an	623±66	8.5±1.4	688	6.9	5.8	717/670 (7)	g, pl, hbl, q
	ab	676±65	9.4±1.4	688	9.8	8.9	650/630 (9.5)	g, pl, hbl, q
MCGM-1B	an	645±59	7.6±1.7	679	6.2	6.4	632/614 (7)	g, pl, hbl, q, bi
	ab	647±58	7.7±1.7	679	6.5	6.7	623/605 (7)	g, pl, hbl, q, bi
MCGM-9	edge	571±96	5.2±1.4	N.A.	N.A.	N.A.	N.A.	g, pl, q, mu, bi, sill
	rim	753±150	9.1±2.3	N.A.	N.A.	N.A.	N.A.	g, pl, q, mu, bi, ky
MCGM-8B	an	581±46	7.5±1.2	657	7.4	6.8	645/627 (7.5)	g, pl, hbl, q, bi, ep
	ab	583±47	7.6±1.2	657	7.8	7.2	641/623 (7.5)	g, pl, hbl, q, bi, ep
MCGM-5†	an	620±37	7.2±1.0	746	8.5	8.4	N.A.	g, pl, hbl, q, mu, bi, ep
	ab	625±41	9.6±1.3	746	12.3	12.5	N.A.	g, pl, hbl, q, mu, bi, ep

Note: Abbreviations: GP 84, Graham and Powell 1984; KS 90, Kohn and Spear 1990 (Fe and Mg endmembers); HB 94, Holland and Blundy 1994; HP 98, Holland and Powell 1998; an, anorthite-rich plagioclase used for calculation; ab, albite-rich plagioclase used for calculation; N.A., not applicable.

*Abbreviations follow Holland and Powell (1998).

†Pownceby et al. (1987) Grt-Ilm thermometer T = 740°C using garnet g437 adjacent to ilmenite inclusion ilhem431.

TABLE 4. U-Th-Pb ISOTOPIC DATA

Spot name	comm 206 (%)	U (ppm)	Th (ppm)	$^{232}Th/^{238}U$	$^{206}Pb/^{238}U$ Age* (Ma, ±1σ)	Total $^{238}U/^{206}Pb$ (± % err)	Total $^{207}Pb/^{206}Pb$ (± % err)	Total $^{208}Pb/^{232}Th$ (± % err)	$^{208}Pb/^{232}Th$ Age† (Ma, ±1σ)
JMDV3 - Monazite									
JMDV3-1	0.02	630	1807	2.97	79.1 ± 0.7	81.0 ± 0.9	0.0478 ± 0.6	0.0039 ± 0.9	77.5 ± 0.7
JMDV3-2	0.06	791	2027	2.65	77.8 ± 0.7	82.3 ± 0.9	0.0481 ± 0.5	0.0038 ± 1.0	75.8 ± 0.7
JMDV3-3	0.13	644	2232	3.58	75.4 ± 0.7	84.9 ± 0.9	0.0486 ± 0.6	0.0037 ± 1.0	74.8 ± 0.7
JMDV3-4	0.05	894	2146	2.48	87.6 ± 0.8	73.1 ± 0.9	0.0481 ± 0.5	0.0043 ± 1.1	86.0 ± 0.8
JMDV3-5	0.33	312	3956	13.11	87.4 ± 0.8	73.0 ± 0.9	0.0504 ± 0.8	0.0044 ± 1.4	88.1 ± 1.0
JMDV3-6	0.03	653	2115	3.35	77.0 ± 0.7	83.2 ± 0.9	0.0477 ± 0.6	0.0038 ± 1.1	75.5 ± 0.7
JMDV3-7	0.13	360	2292	6.58	84.4 ± 0.8	75.8 ± 0.9	0.0487 ± 0.8	0.0041 ± 1.0	82.1 ± 0.8
JMDV3-8	0.14	652	1703	2.70	75.7 ± 0.7	84.6 ± 0.9	0.0486 ± 0.6	0.0037 ± 0.9	74.6 ± 0.7
JMDV3-9	0.10	497	2025	4.21	78.8 ± 0.7	81.2 ± 0.9	0.0484 ± 0.7	0.0039 ± 1.2	78.4 ± 0.8
JMDV3-10	0.19	485	2826	6.02	82.8 ± 0.7	77.2 ± 0.9	0.0492 ± 0.7	0.0040 ± 1.0	79.8 ± 0.8
JMDV3-11	0.29	382	2071	5.60	84.6 ± 0.8	75.5 ± 0.9	0.0500 ± 0.7	0.0042 ± 1.4	85.3 ± 1.1
JMDV3-12	0.05	910	1694	1.92	72.0 ± 0.6	89.0 ± 0.9	0.0479 ± 0.5	0.0036 ± 0.9	71.1 ± 0.7
JMDV3-13	0.07	510	2046	4.14	86.2 ± 0.8	74.3 ± 1.0	0.0483 ± 0.6	0.0042 ± 1.0	83.8 ± 0.9
MCGM12 - Monazite									
MCGM12-1	0.46	313	2163	7.14	96.0 ± 0.9	66.4 ± 0.9	0.0516 ± 0.8	0.0047 ± 1.0	93.7 ± 0.9
MCGM12-2	0.44	385	1221	3.27	95.2 ± 0.9	66.9 ± 0.9	0.0514 ± 0.7	0.0048 ± 1.4	94.6 ± 1.0
MCGM12-3	0.76	235	1393	6.13	94.0 ± 0.9	67.6 ± 1.0	0.0539 ± 0.8	0.0045 ± 1.3	89.1 ± 1.1
MCGM12-4	0.58	286	1552	5.61	83.8 ± 0.8	76.0 ± 0.9	0.0523 ± 0.8	0.0040 ± 1.0	80.8 ± 0.8
MCGM12-5	0.32	243	904	3.84	94.8 ± 0.9	67.3 ± 1.0	0.0505 ± 0.9	0.0046 ± 1.1	92.4 ± 1.0
MCGM12-6	0.46	311	1527	5.07	94.1 ± 0.9	67.7 ± 0.9	0.0516 ± 0.8	0.0046 ± 1.9	90.9 ± 1.3
MCGM12-7	0.21	249	1398	5.81	170.9 ± 1.6	37.1 ± 0.9	0.0512 ± 0.6	0.0084 ± 1.0	168.4 ± 1.6
MCGM12-8	0.51	308	1975	6.62	92.9 ± 0.9	68.6 ± 0.9	0.0519 ± 0.8	0.0045 ± 1.0	91.1 ± 0.9
MCGM12-9	0.37	379	1747	4.76	94.6 ± 0.9	67.4 ± 0.9	0.0508 ± 0.7	0.0046 ± 1.0	91.9 ± 0.9
MCGM12-10	0.32	213	1089	5.29	115.7 ± 1.1	55.0 ± 1.0	0.0509 ± 0.8	0.0056 ± 1.0	112.8 ± 1.2
MCGM12-13	0.56	253	1484	6.06	91.3 ± 0.9	69.7 ± 0.9	0.0523 ± 0.8	0.0045 ± 1.2	88.9 ± 0.9
MCGM12-11	0.33	275	913	3.42	91.5 ± 0.9	69.8 ± 1.0	0.0505 ± 0.8	0.0045 ± 1.3	89.6 ± 1.1
MCGM12-12	0.73	207	2346	11.69	93.4 ± 0.9	68.0 ± 1.0	0.0536 ± 0.9	0.0046 ± 1.7	91.8 ± 1.1

TABLE 4. U-Th-Pb ISOTOPIC DATA (cont.)

Spot name	comm 206 (%)	U (ppm)	Th (ppm)	$^{232}Th/^{238}U$	$^{206}Pb/^{238}U$ Age (Ma, ±1σ)	Total $^{238}U/^{206}Pb$ (± % err)	Total $^{207}Pb/^{206}Pb$ (± % err)	$^{207}Pb/^{235}U$ (± % err)	$^{206}Pb/^{238}U$ (± % err)	err corr
MSG - Zircon										
MSG-1	0.00	17	11	0.66	58.2 ± 3.3	101.5 ± 5.3	0.1118 ± 14.4			
MSG-2	2.59	147	139	0.98	64.7 ± 1.3	97.9 ± 1.9	0.0581 ± 6.0			
MSG-3	6.69	32	21	0.66	73.1 ± 2.3	84.7 ± 3.0	0.0754 ± 9.8			
MSG-4	6.16	43	75	1.78	61.6 ± 1.9	102.4 ± 2.9	0.0605 ± 10.7			
MSG-5	0.00	62	84	1.39	62.4 ± 1.7	100.1 ± 2.6	0.0690 ± 8.3			
MSG-6	0.00	474	566	1.23	62.4 ± 1.1	102.1 ± 1.7	0.0522 ± 3.8			
MSG-7	14.47	57	47	0.85	62.3 ± 2.0	94.7 ± 3.1	0.1130 ± 6.5			
MSG-8	0.00	670	172	0.27	672.2 ± 10.7	8.6 ± 1.6	0.1040 ± 0.7			
MSG-9	0.00	56	107	1.98	61.7 ± 1.6	101.9 ± 2.6	0.0635 ± 8.9			
MSG-10	0.00	12	16	1.30	55.3 ± 3.2	101.3 ± 5.0	0.1517 ± 13.9			
MSG-11	7.34	49	39	0.83	61.3 ± 1.7	103.7 ± 2.7	0.0546 ± 10.1			
MSG-12	0.04	226	51	0.23	1759.2 ± 24.3	3.2 ± 1.6	0.1085 ± 1.0	4.6822 ± 1.9	0.3138 ± 1.6	0.838
MSG-13	0.01	2222	55	0.03	1660.2 ± 18.9	3.4 ± 1.3	0.1031 ± 0.3	4.1718 ± 1.3	0.2937 ± 1.3	0.971
MSG-14	0.00	390	523	1.38	1720.7 ± 19.9	3.3 ± 1.3	0.1035 ± 1.0	4.3649 ± 1.6	0.3059 ± 1.3	0.807
MSG-15	0.00	622	73	0.12	1594.3 ± 18.7	3.6 ± 1.3	0.1044 ± 0.4	4.0399 ± 1.4	0.2806 ± 1.3	0.964
JMDV4 Zircon										
JMDV4-1	3.21	257	39	0.16	1167.0 ± 6.6	5.0 ± 0.6	0.1045 ± 1.0	2.8378 ± 1.2	0.1984 ± 0.6	0.860
JMDV4-2	2.73	320	61	0.20	1530.8 ± 9.3	3.7 ± 0.7	0.1149 ± 1.2	4.3160 ± 2.6	0.2680 ± 0.7	0.841
JMDV4-3	3.41	201	56	0.29	1181.0 ± 11.2	5.0 ± 1.0	0.1039 ± 2.1	2.9450 ± 4.2	0.2011 ± 1.0	0.675
JMDV4-4	0.16	3603	1880	0.54	68.1 ± 0.3	94.0 ± 0.4	0.0486 ± 1.6			
JMDV4-5	1.15	585	22	0.04	1513.8 ± 6.8	3.8 ± 0.5	0.1035 ± 0.9	3.7752 ± 1.0	0.2647 ± 0.5	0.900
JMDV4-6	0.07	322	475	1.52	61.4 ± 0.9	104.3 ± 1.4	0.0478 ± 5.8			
JMDV4-7	4.71	41	17	0.43	678.3 ± 15.0	8.6 ± 2.2	0.1006 ± 3.4			
JMDV4-8	2.13	891	129	0.15	78.0 ± 1.3	80.4 ± 1.6	0.0644 ± 5.7			
JMDV4-9	2.73	75	21	0.29	1009.3 ± 12.7	5.9 ± 1.4	0.0947 ± 2.2	2.2518 ± 2.6	0.1695 ± 1.4	0.690
JMDV4-10	4.99	81	5	0.07	405.6 ± 6.1	15.3 ± 1.5	0.0948 ± 4.7			
JMDV4-11	1.13	873	612	0.72	72.6 ± 0.8	87.2 ± 1.1	0.0564 ± 4.2			
JMDV4-12	4.13	67	33	0.52	51.5 ± 2.5	119.6 ± 4.6	0.0798 ± 13.3			
JMDV4-13	1.07	559	35	0.06	59.8 ± 0.8	106.1 ± 1.4	0.0556 ± 5.3			
JMDV4-14	0.07	1014	337	0.34	57.8 ± 0.5	111.0 ± 0.9	0.0476 ± 3.7			
JMDV4-15	0.16	3241	713	0.23	64.4 ± 0.3	99.5 ± 0.4	0.0486 ± 1.8			
JMDV4-16	1.38	104	319	3.15	62.8 ± 1.6	100.8 ± 2.5	0.0582 ± 9.1			
JMDV4-17	-0.17	1030	433	0.43	62.6 ± 0.5	102.7 ± 0.8	0.0459 ± 3.3			
JMDV4-18	0.16	2731	374	0.14	53.0 ± 0.3	121.0 ± 0.5	0.0483 ± 2.0			

TABLE 4. U-Th-Pb ISOTOPIC DATA (cont.)

Spot name	comm 206 (%)	U (ppm)	Th (ppm)	$^{232}Th/^{238}U$	$^{206}Pb/^{238}U$ Age* (Ma, ±1σ)	Total $^{238}U/^{206}Pb$ (± % err)	Total $^{207}Pb/^{206}Pb$ (± % err)	$^{207}Pb/^{235}U$ (± % err)	$^{206}Pb/^{238}U$ (± % err)	err corr
JC02-MC15 Zircon										
MC15-1	1.46	10716	63	0.01	118.1 ± 0.4	53.3 ± 0.2	0.0600 ± 1.3			
MC15-2	0.23	3562	37	0.01	78.8 ± 0.3	81.1 ± 0.4	0.0494 ± 1.6			
MC15-3	4.77	6186	835	0.14	92.0 ± 0.7	66.3 ± 0.3	0.0857 ± 2.8			
MC15-4	0.29	5438	47	0.01	93.0 ± 0.3	68.6 ± 0.3	0.0502 ± 1.1			
MC15-5	0.05	2749	29	0.01	80.2 ± 0.4	79.9 ± 0.4	0.0480 ± 1.8			
MC15-6	0.13	5048	53	0.01	85.3 ± 0.3	75.0 ± 0.3	0.0487 ± 1.2			
MC15-7	-0.10	7064	161	0.02	87.3 ± 0.4	73.4 ± 0.4	0.0470 ± 2.2			
MC15-8	1.28	4071	64	0.02	89.4 ± 0.4	70.7 ± 0.4	0.0579 ± 1.3			
MC15-9	0.19	4507	49	0.01	87.4 ± 0.3	73.1 ± 0.4	0.0492 ± 1.4			
MC15-10	0.07	6911	86	0.01	85.8 ± 0.3	74.6 ± 0.3	0.0483 ± 1.1			
MC15-11	0.11	13156	158	0.01	88.4 ± 0.2	72.3 ± 0.2	0.0487 ± 0.8			
MC15-12	0.26	5369	58	0.01	84.8 ± 0.3	75.3 ± 0.3	0.0498 ± 1.2			
MC15-13	1.20	4433	32	0.01	86.8 ± 0.5	72.9 ± 0.4	0.0572 ± 4.8			
MC15-14	0.11	4975	53	0.01	81.7 ± 0.3	78.4 ± 0.3	0.0485 ± 1.3			
MC15-15	1.93	6004	73	0.01	105.7 ± 0.5	59.3 ± 0.4	0.0634 ± 2.0			
JC01-MC1 Zircon										
MC1-Z1 rim	0.00	1088	3	0.00	65.1 ± 2.9	97.6 ± 4.5	0.0548 ± 8.3			
MC1-Z2 rim	0.15	1139	8	0.01	300.6 ± 10.1	20.0 ± 3.4	0.0901 ± 0.8			
MC1-Z3 rim	7.68	884	3	0.00	122.7 ± 5.1	50.7 ± 4.0	0.0696 ± 12.5			
MC1-Z4 core	0.06	202	78	0.40	1844.3 ± 61.8	3.0 ± 3.4	0.1096 ± 0.6	4.9619 ± 3.468	0.3298 ± 3.4	0.984
MC1-Z5 rim	2.14	918	3	0.00	83.3 ± 3.5	76.3 ± 4.2	0.0538 ± 5.5			
MC1-Z6 core	0.02	243	129	0.55	2563.8 ± 95.0	2.0 ± 3.4	0.1789 ± 0.3	12.1480 ± 3.424	0.4929 ± 3.4	0.995
MC1-Z7 rim	0.07	1348	10	0.01	566.5 ± 18.8	10.4 ± 3.4	0.0952 ± 0.5			
MC1-Z8 rim	0.00	1611	5	0.00	91.6 ± 3.2	69.8 ± 3.5	0.0487 ± 2.4			
MC1-Z9 rim	0.80	1142	5	0.00	130.6 ± 4.5	48.6 ± 3.5	0.0530 ± 2.9			
MC1-Z10 rim	0.24	1048	4	0.00	336.0 ± 11.4	17.8 ± 3.4	0.0901 ± 1.4			
MC1-Z11 rim	1.03	1432	8	0.01	120.5 ± 4.5	52.6 ± 3.7	0.0554 ± 4.5			
MC1-1 core	0.05	169	115	0.70	2039.5 ± 10.7	2.7 ± 0.6	0.1305 ± 0.7	6.6743 ± 0.9	0.3722 ± 0.6	0.654
MC1-2 core	0.00	1346	64	0.05	394.2 ± 3.0	15.0 ± 0.3	0.0967 ± 0.7			
MC1-3 core	0.01	330	121	0.38	2683.4 ± 9.3	1.9 ± 0.4	0.1821 ± 0.7	12.9581 ± 0.8	0.5163 ± 0.4	0.544
MC1-4 core	0.00	693	177	0.26	1723.7 ± 4.7	3.3 ± 0.3	0.1129 ± 0.4	4.7725 ± 0.5	0.3066 ± 0.3	0.604
MC1-5 core	0.02	209	123	0.61	1952.0 ± 9.5	2.8 ± 0.6	0.1244 ± 1.0	6.0571 1.2	0.3537 ± 0.6	0.482

*^{207}Pb corrected ages for grains <1000 Ma, ^{204}Pb corrected ages for grains >1000 Ma

†^{204}Pb corrected

Sample: -> *02MC4 hbl*

A

T	t	40(mol)	40/39	37/39	36/39	K/Ca	∑ 39Ar	40Ar*	Age (Ma)
800	*12	8.1691E-14	73.8283	1.3542	0.1656	0.361	0.0551003	33.8%	**47.9 ±1.8**
900	*12	3.7887E-14	22.9526	1.5646	0.0336	0.313	0.1373584	57.2%	**25.3 ±0.9**
1000	*12	2.04E-14	21.0066	0.7481	0.0244	0.655	0.1857901	65.9%	**26.7 ±1.0**
1050	*12	2.9099E-14	19.2973	2.6998	0.0186	0.181	0.2608858	72.5%	**27.0 ±0.7**
1100	*12	4.4296E-14	15.8493	1.7302	0.0137	0.283	0.400226	75.1%	**23.0 ±0.4**
1125	*12	4.5499E-14	14.8619	2.8180	0.0098	0.173	0.5527414	81.9%	**23.5 ±0.3**
1150	*12	4.9148E-14	13.0149	4.5147	0.0058	0.108	0.7406641	89.2%	**22.5 ±0.3**
1175	*12	4.8745E-14	15.2889	5.2118	0.0070	0.094	0.8991775	88.7%	**26.2 ±0.4**
1200	*12	3.5763E-14	18.4442	5.5891	0.0093	0.087	0.9955196	87.1%	**31.1 ±0.5**
1250	*12	4.0801E-15	59.2585	5.4261	0.0007	0.090	0.9989373	100.3%	**112.4 ±11.6**
1300	*12	2.0594E-15	96.3607	3.0251	0.2666	0.162	1	18.4%	**34.3 ±27.4**

B — *ellipses are 2σ*

02MC4 hornblende
Age = 21.7 ± 1.1 Ma
40/36 intercept: 386 ± 58
MSWD = 3.4

$^{36}Ar/^{40}Ar$ vs $^{39}Ar/^{40}Ar$

C — *box heights are 2σ*

Age (Ma) vs Cumulative ^{39}Ar Fraction

D — *box heights are 2σ*

K/Ca vs Cumulative ^{39}Ar Fraction
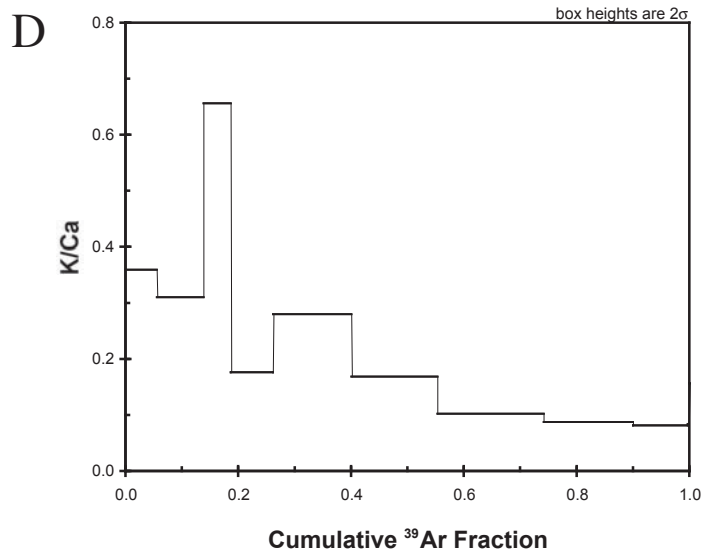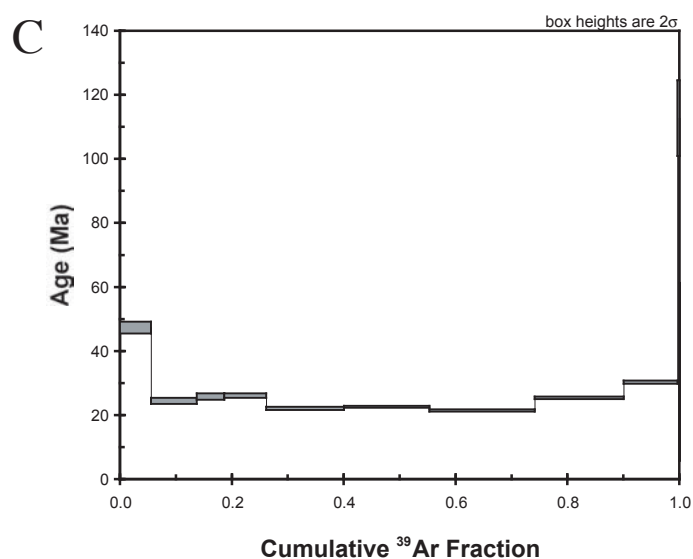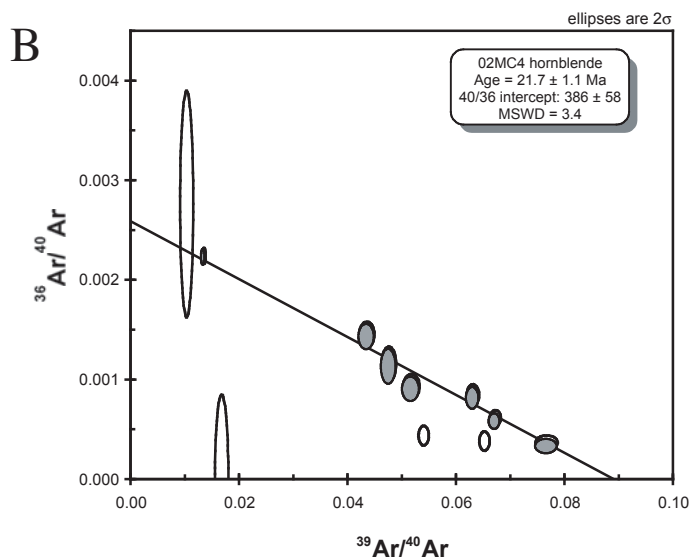
Data table (A), inverse isochron diagram (B), age spectra (C), and K/Ca diagram from $^{40}Ar/^{39}Ar$ analysis of hornblende separates from sample JC02-MC-4, a steeply-dipping mafic dike in Monarch Canyon which cuts all fabrics and is itself brittley offset a few meters by the Monarch Spring fault. A non-atmospheric $^{40}Ar/^{36}Ar$ intercept of 386 ± 58 indicates significant excess argon, a feature very common in analyses from the Funeral Mountains. Isochron age was calculated without the highest temperature, lowest K steps. Outcrop location is latitude 36° 43.419' N and longtitude 116° 55.353'W.

MC-DR1.ai
Mattinson, Colgan, Metcalf, Miller, and Wooden